MHD-blob correlations in NSTX F

S. J. Zweben (iD), E. D. Fredrickson (iD), J. R. Myra (iD), M. Podestà (iD), and F. Scotti (iD)

COLLECTIONS

F   This paper was selected as Featured

View Online   Export Citation   CrossMark

Physics of Plasmas

AIP Publishing

MHD-blob correlations in NSTX ⓕ

View Online　　Export Citation　　CrossMark

S. J. Zweben,[1,a) ⓘ E. D. Fredrickson,[1] ⓘ J. R. Myra,[2] ⓘ M. Podestà,[1] ⓘ and F. Scotti[3] ⓘ

AFFILIATIONS

[1]Princeton Plasma Physics Laboratory, Princeton New Jersey 08540, USA
[2]Lodestar Research Corporation, Boulder, Colorado 80301, USA
[3]Lawrence Livermore National Laboratory, Livermore, California 94550, USA

a)Author to whom correspondence should be addressed: szweben@pppl.gov

ABSTRACT

This paper describes a study of the cross-correlations between edge fluctuations as seen in the gas puff imaging (GPI) diagnostic and low frequency coherent magnetic fluctuations (MHD) in H-mode plasmas in NSTX. The main new result was that large blobs in the scrape-off-layer were significantly correlated with MHD activity in the 3–6 kHz range in 21 of the 223 shots examined. There were also many other shots in which fluctuations in the GPI signal level and its peak radius Rpeak were correlated with MHD activity but without any significant correlation of the MHD with large blobs. The structure and motion of the MHD are compared with those of the correlated blobs, and some possible theoretical mechanisms for the MHD-blob correlation are discussed.

Published under license by AIP Publishing. https://doi.org/10.1063/5.0006515

I. INTRODUCTION

Blobs are discrete high-density plasma structures, which are born in the edge regions of tokamaks and which carry particles and heat across the edge and scrape-off-layer (SOL) plasmas.[1–4] These blobs (also known as edge filaments) are therefore important in determining the pattern of heat and particle fluxes to the wall and divertor plate and also for affecting the transport of impurities between the wall and the main plasma.

The present paper describes evidence for a new phenomenon in which large blobs at the edge of the NSTX tokamak are significantly cross-correlated with low frequency coherent magnetic fluctuations measured near the outer midplane, which for brevity we refer to here as "MHD." This result is surprising since MHD modes usually have a global (full-torus) structure in space and are periodic in time, whereas blobs have a much smaller (mesoscale) structure and are randomly distributed in time. As far as we know, this correlation of coherent magnetic fluctuations and blobs has not been observed previously or predicted theoretically in a tokamak.

Blobs in tokamaks are normally created near the magnetic separatrix or last closed flux surface where large edge density gradients and strong turbulence are present. For example, in the JET tokamak, blobs and their associated negative-density holes were born in the edge shear layer just inside the separatrix,[5] and in the HL-2A tokamak, blobs were also born just inside the separatrix where the density gradient was maximum and the turbulence skewness was near zero.[6] In the NSTX tokamak, blobs are born in the edge with a density and

temperature characteristic of the plasma conditions where underlying linear edge drift-curvature instabilities are localized.[7]

Blob generation has also been measured in other types of magnetized plasmas. For example, in the TJ-K stellarator, blobs were generated by drift-wave turbulence near the last closed flux surface in regions of negative mean normal curvature,[8] and blobs in the simple torus TORPEX were observed to form from radially extending positive crests of the interchange waves that are sheared off by the E × B flow.[9] These experimental results[5–9] suggest that blobs are generated by electrostatic drift-wave or interchange instabilities combined with local flow shear, both of which can be strong in the edge region due to the large density and/or temperature gradients. These experimental results have been compared at least qualitatively with analytical and numerical computations of blob formation based on electrostatic instability models,[4,10–12] as discussed further in Sec. IV D.

The first numerical computations of blob formation and propagation were carried out in two-dimensions perpendicular to the magnetic field, assuming approximately constant conditions along both the blob-filament and the background magnetic field, as discussed in Ref. 4 (and references therein). Blob emission triggered by large scale plasma transients was observed in the simulations of Ref. 13. More recently, a number of three-dimensional codes have been employed to study blob formation and evolution using both fluid[14–17] and kinetic[18,19] models. The models are increasing in realism, incorporating effects such as X-point geometry[15] and neutral-plasma interactions.[20–22] Nevertheless, the basic idea remains that blobs form in the

presence of edge turbulence and are propelled radially by interchange forces (i.e., curvature and grad-B drifts creating an effective acceleration $g \sim c_s^2/R$), which give rise to internal charge polarization of the blob and a subsequent radial $E \times B$ drift. These concepts will be employed in Sec. IV D where possible interaction mechanisms between MHD modes and blobs will be discussed. To the best of our knowledge, no simulations to date have studied the interaction of MHD modes with blobs.

Related, purely theoretical investigations have been carried out. Of particular relevance to the present paper are theories describing the interaction of background modes with blobs.[23,24] These endeavors have so far only considered how small-scale background turbulence participates in blob formation through wave-wave coupling and modulation instability; however, a similar wave-coupling approach may shed light on how large-scale modes can interact with blobs.

MHD modes are large-scale coherent magnetohydrodynamic plasma oscillations, which are seen in all tokamaks. In general, MHD modes can be driven by gradients in plasma pressure, current density, or energetic particles and can be diagnosed using external magnetic field sensor coils, x-ray emission from the core, or emission or reflection of microwave radiation. The MHD modes discussed in this paper were measured using external magnetic coils located near the outer midplane, and their correlation with blobs is examined in the low frequency range of 1–10 kHz, which is in the range of blob lifetimes in NSTX. Typical toroidal MHD mode numbers were $n = 3$–5, with the dominant mode of $n = 4$. Based on comparison with earlier measurements (see below), these MHD modes were localized in the edge pedestal region of H-mode plasmas.

Although MHD-correlated blobs have not, to our knowledge, been observed previously, the present results may be related to previous experimental work on the interaction between small-scale turbulence and larger-scale coherent modes. For example, blob creation associated with an $m = 1$ electrostatic (not MHD) mode was observed in the linear device CSDX,[25] and the correlation of MHD activity with edge electrostatic turbulence (although not blobs) was observed during lower hybrid current drive experiments in the HT-7 tokamak.[26] The blob frequency and blob transport were reduced with the application of (static) external $m/n = 6/2$ or 3/1 resonant magnetic perturbations in the TEXTOR[27] and J-TEXT tokamaks.[28] A correlation between externally imposed rotating magnetic islands and edge turbulence was studied in the RFX-Mod reversed field pinch, where local vorticity was suggested as the interaction mechanism.[29] In a wider context, the multi-scale interaction of core neoclassical tearing modes with local turbulence has been observed and modeled in DIII-D.[30] In theory, edge turbulence can also generate seed magnetic islands on low order rational surfaces,[31] possibly causing MHD modes.

From the perspective of edge MHD modes in tokamaks, this work is most closely related to a previous paper, which showed SOL heat flux broadening due to edge harmonic oscillations (EHOs) just inside the separatrix in NSTX.[32] However, that paper focused on counter-rotating edge MHD modes that were seen in the GPI view as upward propagating structures near the separatrix, whereas the present paper focuses on co-rotating MHD structures that are correlated with blobs that propagate downward in the SOL. Co-propagating EHO-like structures have also been observed in NSTX,[33] in JET as a "current ribbon" at the top of the H-mode pedestal,[34] and in quiescent QH-mode discharges with EHO modes in DIII-D.[35,36] However, in none of these studies were the EHO-like modes observed to be correlated with SOL blobs.

The present paper aims to show examples of a new phenomenon in which MHD activity seen in the magnetic pickup coils is significantly correlated with SOL blobs as seen by GPI in NSTX. However, a complete characterization of this MHD activity is beyond the scope of the present paper. This paper is organized as follows: Sec. II describes the GPI and MHD diagnostics and database used in this paper, Sec. III describes the experimental results, Sec. IV is a discussion of these results and their theoretical interpretation, and Sec. V contains a Summary and Conclusion. There are also two Appendixes: Appendix A describes the blob tracking algorithm and Appendix B describes the MHD-blob cross-correlation analysis.

II. DIAGNOSTICS AND DATABASE

The gas puff imaging (GPI) diagnostic of NSTX has been described in several recent papers,[37–39] so only a brief summary is presented here. A photograph of the GPI diagnostic geometry is shown Fig. 1, along with the B-dot coil used to measure the MHD activity.

In GPI, a fast camera (Vision Research Phantom 710) views a deuterium neutral gas cloud puffed into the plasma, using a $D\alpha$ filter to image a neutral deuterium emission line during the steady-state part of the discharge. This neutral gas cloud increases the $D\alpha$ emission in the camera line of sight by a factor of at least $\times 10$ over a distance of ~ 12 cm along the B field line,[39] which localizes this line emission to the region near the gas puffer. The camera viewing angle is as near as possible aligned along the local magnetic field, which is tilted at an angle of $36°$ with respect to the toroidal direction, resulting in images of the local $D\alpha$ light emission from the cloud, which are approximately radial (i.e., perpendicular to the local separatrix) vs poloidal (i.e., along the local separatrix) planes with 64×80 pixels at 400 000 frames/s (2.5 μs/frame). The GPI camera frame covers an area 24 cm radially and 30 cm poloidally centered ~ 20 cm above the outer midplane[37–39] near the separatrix. Most of this GPI light emission occurs within
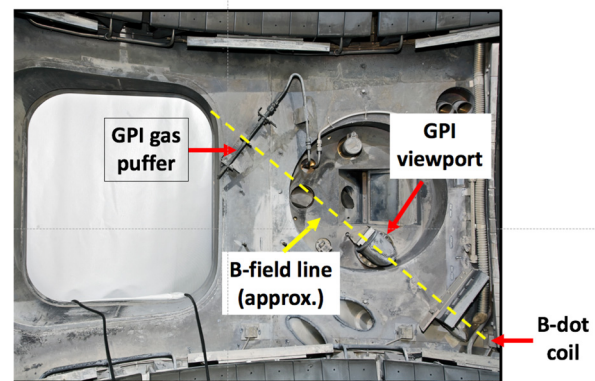
FIG. 1. Photograph inside the NSTX vessel showing the GPI diagnostic geometry and the B-dot coil used for analysis in this paper. The $D\alpha$ light emission from the GPI gas puffer located just above the outer midplane was viewed from the GPI viewport located just below the outer midplane. The B-dot coil was below the outer midplane at the wall $\sim 30°$ toroidally from the GPI gas puffer. This coil was chosen to be as close as possible to the magnetic field line going through the GPI gas cloud, as indicated (approximately) by the yellow dashed line.

± 5–10 cm of the separatrix, where the electron temperature is high enough to excite the Dα line but low enough so that the neutrals are not completely ionized (typically within $T_e \sim$ 10–200 eV). The GPI gas puff in NSTX occurs over $\sim$50 ms, but for this paper, only 10 ms near the time of peak signal is analyzed.

The Dα light emission seen in GPI fluctuates due to the local electron density and temperature variations, including both turbulent and coherent (i.e., MHD) fluctuations. Thus, it is not surprising that the GPI signal fluctuates in phase with an edge MHD mode; however, it is surprising that localized blobs are correlated with the large-scale MHD, which motivates this paper.

Various issues and assumptions in the interpretation of these GPI images were discussed in a recent diagnostic review paper.[40] For example, the present blob analysis is done using the Dα light emission images with no attempt to unfold the underlying electron density fluctuations, and the spatial resolution of the system can be affected by slight misalignments of the camera view with respect to the local field line. The neutral density fluctuations due to the turbulence itself might affect the space-time structure of the Dα line emission, and the GPI data alone are not sufficient to determine turbulent transport since the density and radial velocity fluctuations are not directly measured. However, the present GPI analysis is well suited for the identification of blobs and coherent edge fluctuations within its field of view.

The MHD data used in this paper came from a single magnetic field fluctuation sensor (Mirnov coil HN0), which measured the rate of change of the vertical magnetic field (B-dot signal). This coil was located $\sim$50 cm below the outer midplane and $\sim$30° toroidally from the GPI image plane, as illustrated in Fig. 1. The location of this coil was chosen to be as close as possible to the magnetic field line going through the GPI gas cloud center, as indicated in Fig. 1. This coil was located on the vessel wall at a distance of about $\sim$1.2 m from the GPI gas cloud and approximately along the angle of the GPI view (36° vertically). This coil location produced the highest cross-correlations with blobs seen in GPI among a toroidal array of similar coils at the same height (see Sec. IV E). The frequency response of these coils was over 1 MHz, but the B-dot data for this paper were bandpass filtered to within a frequency range of 1–10 kHz, in which the MHD period was comparable to the $\sim$100 μs lifetime of the blobs. The small hardware timing difference between the GPI camera and B-dot coils was not measured directly, but the maximum cross correlations were evaluated using a much larger variable lag time of up to ± 500 μs. There was no effect of the GPI gas puff on the magnetic signals analyzed in this paper.

Typical parameters for the NSTX database used in this paper are shown in Table I, including plasma current I_p, toroidal field B_t, line-averaged electron density n_e, total stored energy W_{mhd}, and neutral beam injection (NBI) power P_{nb}. The first two columns describe the shots from 2010 runs that are used in Secs. III B–III F to illustrate the MHD-blob correlation phenomenon. The left column is for a set of 7 similar shots selected to have a "high MHD-blob correlation," and the middle column is for a different set of 7 similar shots selected to have a "low MHD-blob correlation." These two sets of shots are in H-mode and Ohmic plasma states, respectively; however, not all H-mode shots have a high MHD-blob correlation. These are the same shots used previously to study the statistics of blobs in H-mode shots and Ohmic plasmas,[38] but the correlation between MHD activity and large blobs in the H-mode shots was not noticed at that time.

A wider database of 223 shots with GPI data from the same run is discussed in Sec. III G, with parameters shown in the right column of Table I. These 223 shots include all the available shots with both GPI blob data and MHD data from 2010, and represent the general behavior of NSTX shots from this run. These include 40 Ohmic shots with auxiliary power $P_{tot} <$ 0.1 MW, 117 shots with $P_{tot} >$ 2 MW (which are mostly in H-mode), and 66 shots with $P_{tot} =$ 0.1–2 MW, which are a mixture of L-mode and H-mode plasmas. The auxiliary power included RF on 28 shots and NBI on 154 shots.

III. EXPERIMENTAL RESULTS

The main goal of this section is to describe experimental results that demonstrate a cross correlation between large blobs as seen in the GPI signal and MHD activity as seen in the magnetic sensors. To gradually and systematically lead up to this result, we will present three different types of cross-correlation analyses for each of three different datasets. Subsection III A gives an overview of the data and analysis in Sec. III. Discussion of the physical interpretation of these results is presented in Sec. IV.

A. Overview of data and analysis

We use three different types of cross-correlation analyses in this section. The first two correlation analyses compare the GPI signal level and its peak radius to the MHD signals, while the third (and most interesting) correlation analysis compares the large blobs with the MHD signals. We also use three different datasets to systematically present the results. The first dataset contains just two sample shots for

TABLE I. NSTX parameters.

	High MHD-blob corr.	Low MHD-blob corr.	223 shot database
Shot type	H-mode	Ohmic	Mixed
Shot # range	140389–395 (7 shots)	141746–756 (7 shots)	137582–142275
Time (ms)	532–547	212	128–814
I_p (kA)	830	830	600–1200
B_t (kG)	4.9	3.6	3.4–5.4
n_e (cm^{-3})	5.2×10^{13}	1.6×10^{13}	1.3–7.2×10^{13}
W_{mhd} (kJ)	220	32	18–344
P_{nb} (MW)	4.0	0	0–6.0
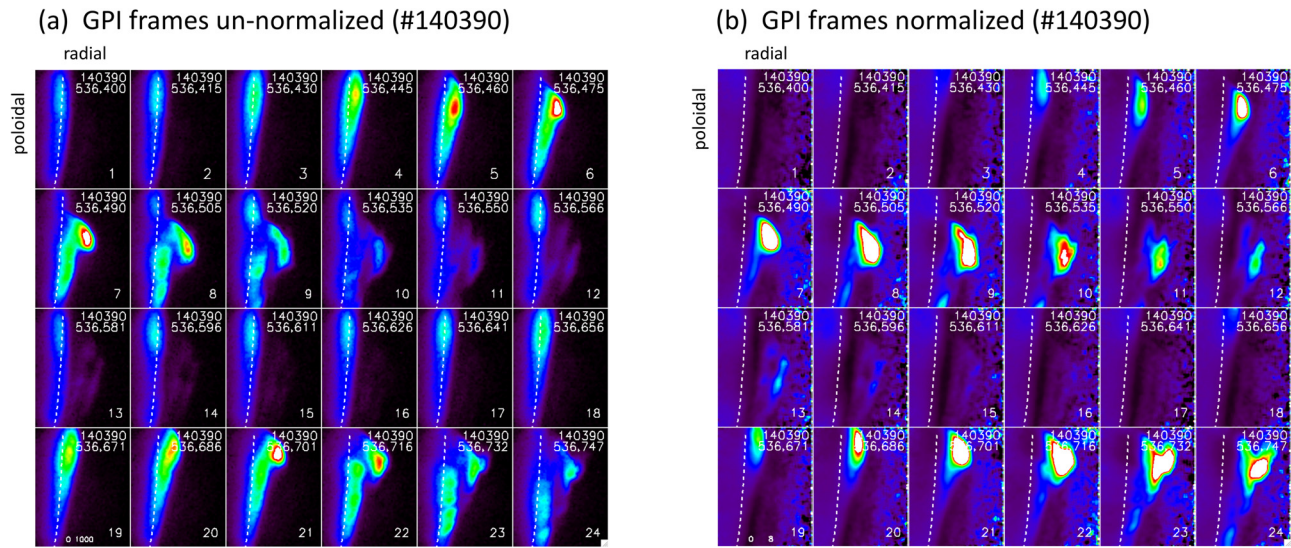
FIG. 2. An example of showing the 2D motion of large blobs within the GPI camera view during a shot with high MHD-blob correlation (#140390). Each frame covers 24 cm radially (horizontal) and 30 cm poloidally (vertical), with 15 μs (6 camera frames) between each image. The images in (a) are un-normalized raw camera data, while the images in (b) are normalized by a time-average image and plotted with a color scale ranging from 0 (black) to 8 (white), with 4–6 as green. The separatrix is shown by the dashed line, the radially outward direction is to the right, and the downward blob motion is in the ion diamagnetic direction.

illustration, the second dataset contains 7 similar shots of each of these types to demonstrate the reproducibility of these results, and the third dataset has the widest possible sample of 223 shots from the 2010 NSTX run (see Sec. II).

We start in Sec. III B with an example of the raw GPI imaging data that are the basis of this analysis. The example used in Fig. 2 is chosen from a shot that will later be shown to have large blobs correlated with MHD activity. Section III C and Figs. 3–5 give initial evidence for the cross correlations between the GPI signal level and its peak radius with the MHD signal for the shot of Fig. 2 and compare this with a shot that does not show such correlations. Note that these two cross correlations are made using the GPI signals but not yet using the large blobs. Section III D and Fig. 6 define the large blobs in the context of this paper and illustrate their trajectories for the two sample shots, while Fig. 7 of Sec. III D shows the good reproducibility of these blob velocities for the 7 similar shots of each type. Note that these two sets of seven shots were previously used for a study of blob statistics in NSTX,[38] so the previous detailed description of the blob statistics and profiles can be applied in the present paper.

Section III E presents the most important result of this paper, namely, the correlation between large blobs and MHD activity. Figure 8 illustrates this correlation using the two sample shots of Fig. 3, and Fig. 9 shows the periodicity of these large blobs at the MHD frequency. Figure 10 shows explicitly a cross-correlation function between large blobs and the MHD signals for the two sample shots (i.e., the "blob-bdot correlation"), and Fig. 11 gives all three cross-correlation coefficients for the 7 similar shots of each type, again showing their good reproducibility. Section III F shows (for the sake of completeness) the variation of the blob-bdot correlation as a function of the blob threshold amplitude. Finally, Sec. III G presents all three GPI vs MHD cross-correlation coefficients for the wider database of 223 shots in Fig. 12,

along with various parameter scaling trends in Fig. 13 and a few examples from the wider database in Fig. 14.

Since the description of these correlation results is the main goal of this Sec. III, we chose *not* to present in this section the MHD mode spectra and toroidal mode structure but instead point the interested reader to Sec. IV A and Figs. 15 and 16 for a discussion of these data in connection with the physical interpretation of these results. As mentioned in the Introduction, the MHD modes in the relevant range of 1–10 kHz have a toroidal MHD mode number in the range n = 3–5 and are localized in the edge pedestal region. Although clearly relevant, a full characterization of the MHD activity is beyond the scope of the present work, except for the limited information in Sec. IV A.

B. Example of large blob formation during MHD activity

Figure 2 shows a time sequence of 24 GPI image frames of Dα emission over 350 μs for a shot with MHD activity (#140390). The same frames are shown in both Figs. 2(a) and 2(b), but those in (a) are un-normalized raw camera data, while those in (b) are normalized (i.e., divided by) the time-averaged frame over 10 ms. The time separation between images for both is 15 μs (i.e., 6 camera frames), and the spatial scale of each frame is 24 cm radially (i.e., horizontal) by 30 cm poloidal (vertical). The color scale in Fig. 2(a) is linear with black-to-white ranging from 0 to 1000 counts, and for the normalized images in Fig. 2(b), it is linear from 0 to 8, where white is 8 and green is $\sim$4–6. The magnetic separatrix (EFIT02) is shown by the dashed white line.

The first large blob in this sequence can be seen most clearly in the normalized images of Fig. 2(b), starting at the top of frame #4 just outside the separatrix and ending about frame #12, during which its peak normalized amplitude is always above 4 (green) and often above 8 (white). This blob moves downward poloidally (ion diamagnetic

(a) high MHD-blob correlation (#140390)   (b) low MHD-blob correlation (#141749)
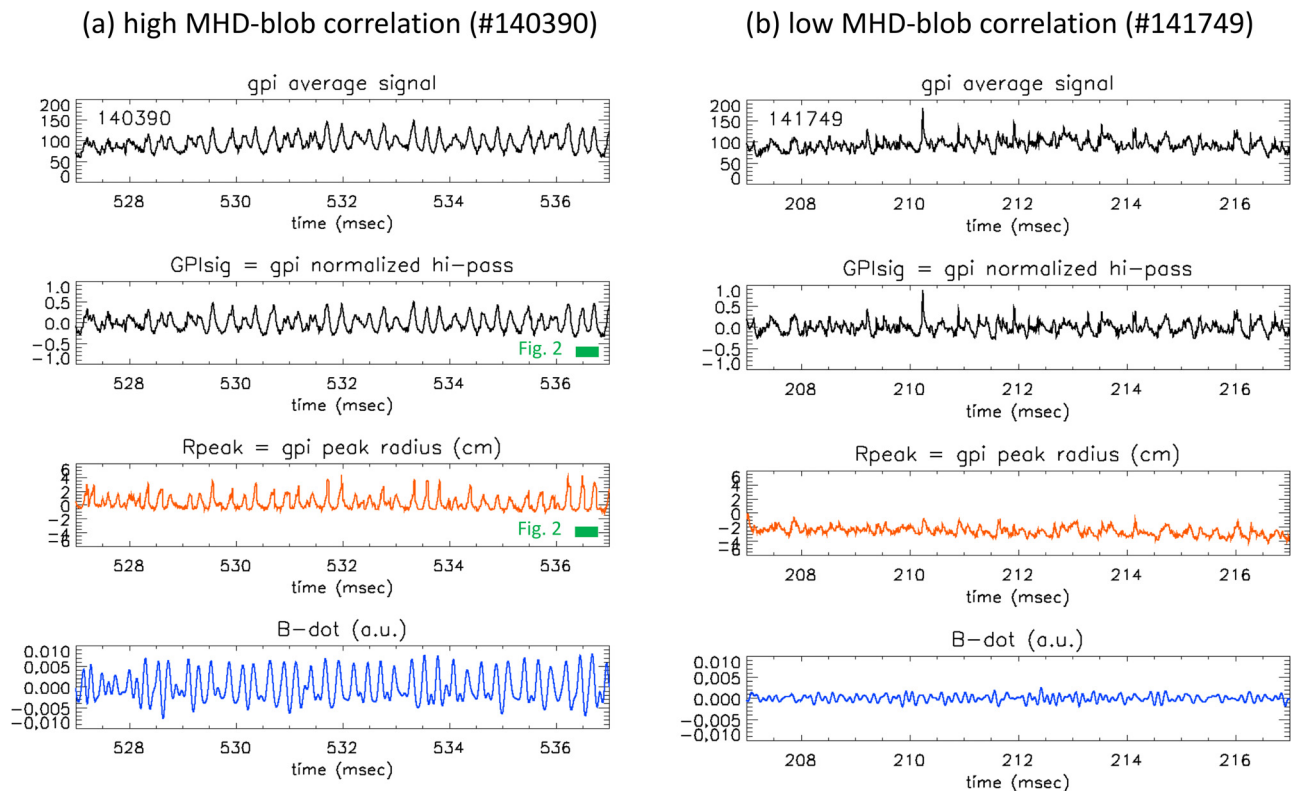
FIG. 3. Comparison of GPI and B-dot signals from two shots, the one at the left in (a) with high MHD-blob correlation (#140390) and the one at the right in (b) with low MHD-blob correlation. The timescale shown for both cases is 10 ms near the peak of the GPI gas puff. The top panel shows the time dependence of the average GPI signal levels over the entire frame, and the second panel shows the same signals after high-pass filtering and normalization (GPIsig). The third panel (red) shows the radial location of the peak of the GPI signals measured with respect to the local separatrix (Rpeak), and the bottom panel (blue) shows the B-dot signal level, after filtering between 1 and 10 kHz. There are clear modulations in the GPIsig and Rpeak signals along with the B-dot signals at ∼4 kHz in shot (a), while there are no clear coherent oscillations in shot (b).

direction) and outward radially for about $100\,\mu s$. A second large blob starts at about frame #19 and also moves downward and outward through the last frame in this sequence. The time between the start of these two blobs is close to the MHD period, as discussed below. Note that the normalized amplitude, area, and shape of these large blobs vary considerably over their lifetime.

C. Evidence for correlation of the GPI signal with MHD activities

Figure 3 compares GPI and MHD signals from two different shots, one shot with a "high MHD-blob correlation" in Fig. 3(a) (#140390) and the other with a "low MHD-blob correlation" in Fig. 3(b) (#141749). The actual calculation of the MHD-blob correlations will be discussed in Sec. III E, but for the moment, these shots will be referred to this way without yet specifying the magnitude of these correlations. These data are shown for a 10 ms period near the peak of the GPI gas puff, which occurred during the steady-state, constant current portion of these discharges. The shot in (a) is a NBI-heated H-mode plasma, and the shot in (b) is an Ohmic plasma (see Table I for parameters). The overall blob statistics in similar shots were discussed in detail in Ref. 38.

The top panels in (a) and (b) of Fig. 3 show the time dependence of the GPI signal level averaged over the entire image frame (see Fig. 2), and the second panels show a high-pass version of this signal after a smoothed version (by 200 frames or 0.5 ms) was subtracted, followed by normalization (division by) the smoothed signal. This normalized high-pass version of the total GPI light emission vs time will be called "GPIsig" below. For the shot with a high MHD-blob correlation in Fig. 3(a), these second panels show a coherent fluctuation at ∼4 KHz with a modulation amplitude of about ±30% (peak-to-peak), while for case with a low MHD-blob correlation in Fig. 3(b), there are large but random-looking fluctuations with no clear period. The third panels (in red) show the radial (i.e., horizontal) location of the peak of the GPI signals measured with respect to the local separatrix, averaged over vertical image rows 10–70 (of 80). This radial location of the peak GPI signal with respect to the separatrix vs time will be called "Rpeak" below. These modulations in "GPIsig" and "Rpeak" can also be seen in the images of Fig. 2(a), where the time range of Fig. 2 is shown by the small green boxes in the middle panels of Fig. 3(a).
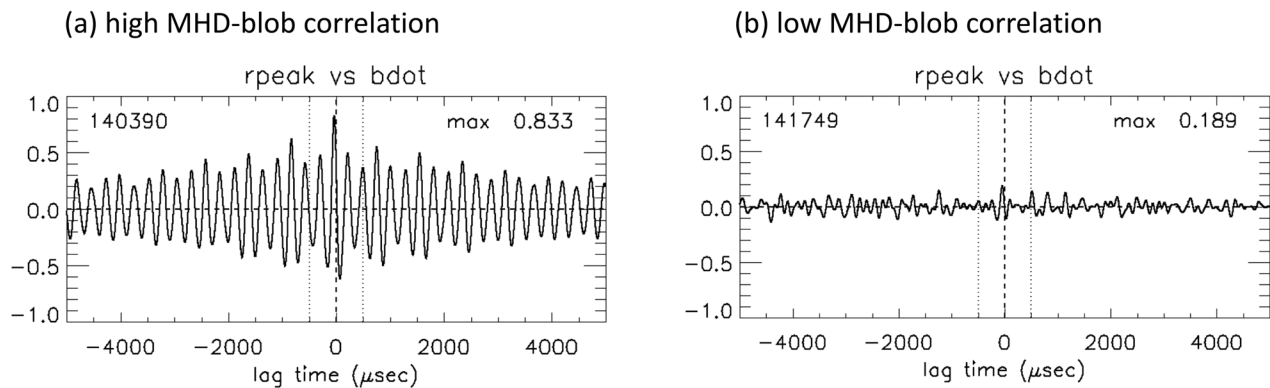
For the case with a high MHD-blob correlation in Fig. 3(a), there is a near-periodic modulation of up to ∼4 cm (peak-to-peak) in the radial location of the peak GPI signal location, while in Fig. 3(b) with a low MHD-blob correlation, there is no such modulation. The bottom

(a) high MHD-blob correlation
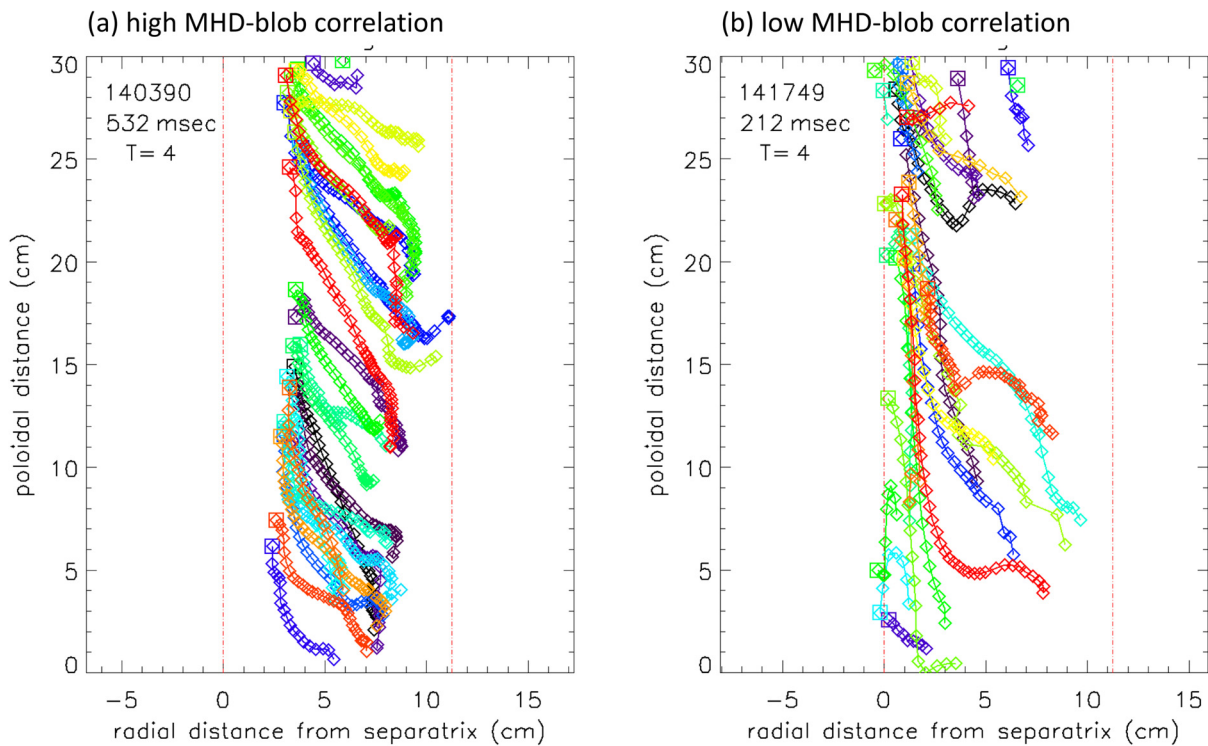
(b) low MHD-blob correlation
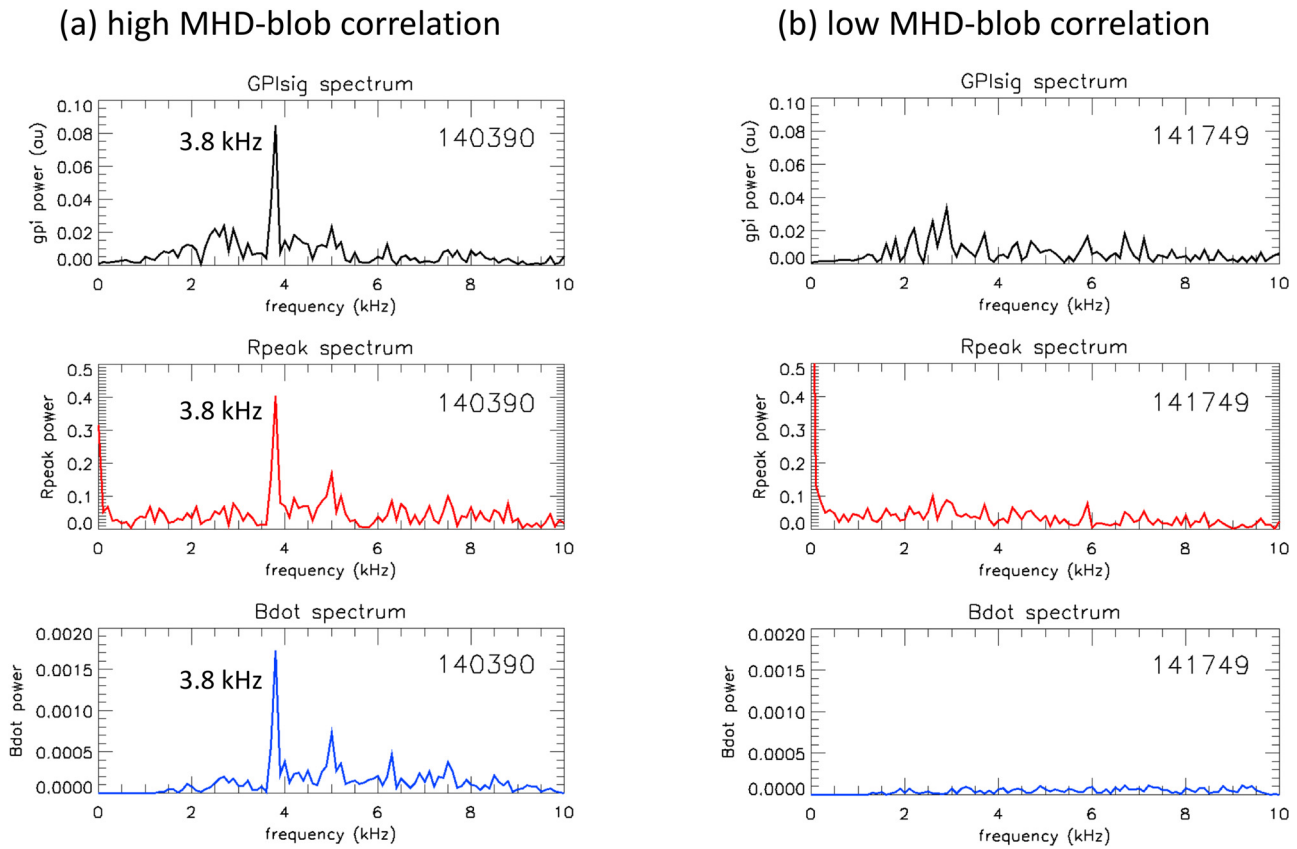
FIG. 4. Power spectra vs frequency within 1–10 kHz for the second and third and fourth panels in Fig. 2 for both shots. For (a) with high MHD-blob correlation, there is a clear peak at 3.8 kHz in the GPI signal level "GPIsig" (top), the GPI peak radius "Rpeak" (middle), and the B-dot signal (bottom), but there are no clear peaks in the shot low MHD-blob correlation in (b).

panels of Fig. 3 (blue) show the magnetic fluctuation (or "B-dot") signal from the coil nearest to the GPI diagnostic along a B-field line (see Sec. II), after filtering within a frequency range of 1–10 kHz. There are clear modulations in the B-dot signal at ~4 kHz in (a), while there are

no clear coherent oscillations in (b). Thus, Fig. 3 shows evidence for an oscillation in both the GPI signal amplitude and the GPI radial peak location at nearly the same the frequency as the MHD activity. Although such an MHD-induced modulation has not been

(a) high MHD-blob correlation

(b) low MHD-blob correlation

FIG. 5. Cross-correlation function between the GPI peak radius (Rpeak) signals and B-dot signals used for the spectra of Fig. 3. The peak of the cross-correlation function (within a lag time range of ±500 μs) for the shot high MHD-blob correlation in (a) was is 0.83, while the peak for the shot with low MHD-blob correlation in (b) was only 0.19. There is a clear oscillating cross-correlation function in (a) with a period of ~0.26 ms (3.8 kHz), while there is no clear oscillation in the cross-correlation function of the shot in (b) without low MHD-blob correlation. This demonstrates the correlation between the GPI signals and MHD signals in the shot with high MHD-blob correlation in (a).

FIG. 6. Large blob tracks for 10 ms periods in shots (a) with high MHD-blob correlation (#140390) and (b) with low MHD-blob correlation (141749). For both cases, the blob trigger threshold was at a normalized amplitude of T = 4. The first frame in each track is marked with a square, and the subsequent symbols are separated by 1 frame (2.5 μs). The radial distance is measured with respect to the local separatrix, and the vertical dashed lines show the radial range over which the search is made for the blob trigger. There were 27 blob tracks in (a) and 25 tracks in (b), all of which moved radially outward to the right and almost all of which moved downward (ion diamagnetic drift direction). The blob tracks were strikingly self-consistent for the shot with high MHD-blob correlation.
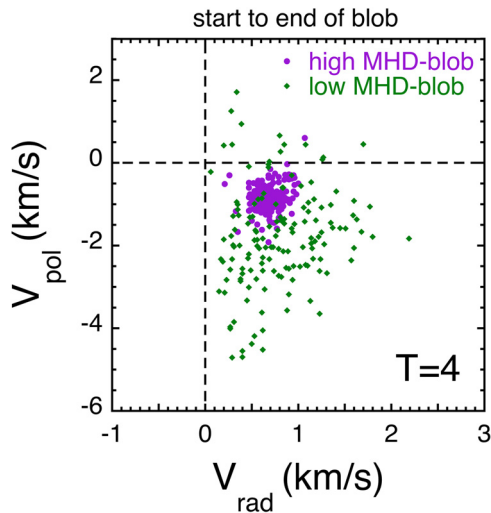

FIG. 7. Average radial vs poloidal velocities for all large blobs in 7 H-mode shots high MHD-blob correlation (purple) and seven shots with low MHD-blob correlation (green). For all cases, the blob trigger threshold was at a normalized amplitude of T = 4. Each point represents the average velocity from the start point to the end point of a single blob. These average velocities are much more self-consistent for the shots with high MHD-blob correlation.

documented previously for NSTX GPI data, it is relatively common and not too surprising since an edge MHD mode will modulate the local electron temperature and density profiles, which will then modulate the GPI amplitude and radial profile (see Sec. IV B).

Figure 4 shows the frequency spectra within the range of 1–10 kHz for the second (GPI signal), third (GPI peak radius), and fourth (B-dot) panels of Fig. 3 for both shots. This frequency range was chosen to match the measured blob lifetime of ~100 μs and excludes a stronger higher frequency mode at ~16 kHz, which is not correlated with blobs (see Sec. IV A). For the shot with a high MHD-blob correlation in Fig. 4(a), there is a dominant peak at 3.8 kHz in the power spectrum of the GPI signal (top), the GPI peak radius (middle), and the MHD signal (bottom), with smaller peaks at ~5 and 2.5 kHz. However, for the shot with a low MHD-blob correlation in Fig. 4(b), there are no dominating peaks in either the GPI or MHD spectra in this frequency range.

Figure 5 shows the cross-correlation function between the GPI peak radius (Rpeak) signals and B-dot signals used for the spectra of Fig. 4. Both signals were re-binned into 10 000 point time series (1 μs/step) to perform this correlation. The peak of the cross-correlation function for the shot with a high MHD-blob correlation in (a) is relatively high (0.83; within a ±500 μs lag time), while the peak for the shot with a low MHD-blob correlation in (b) is relatively small (0.19). There is clearly an oscillating cross-correlation function in (a) with a
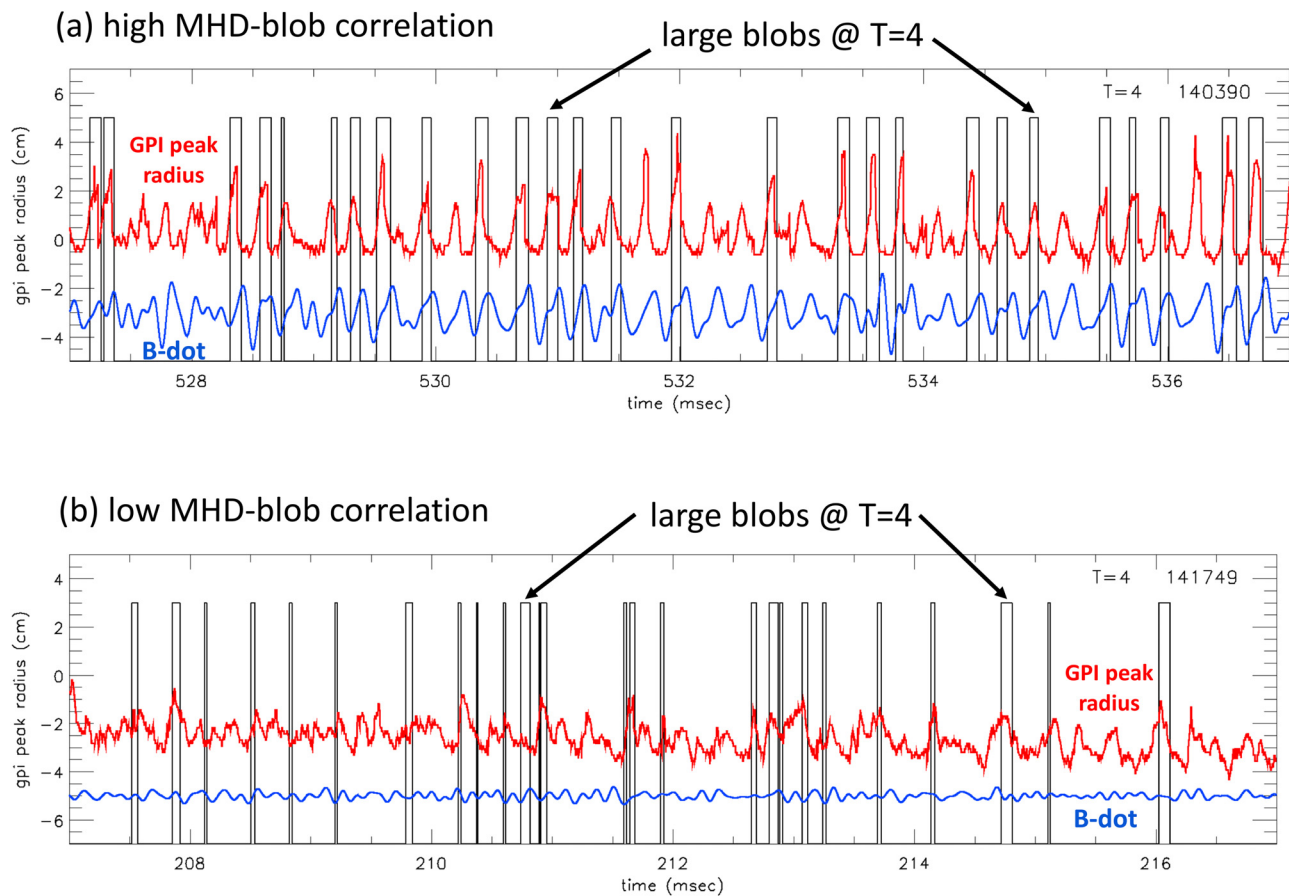
FIG. 8. Timing of blob events (black on/off pulses) along with the B-dot (blue) and peak GPI radius Rpeak (red) signals for the two shots in Fig. 6. The 27 large blobs in Fig. 8(a) with high MHD-blob correlation all occur near a local maximum in the radius of the peak GPI signal and have a periodicity similar to the B-dot signal. The 25 large blobs in the shot with low MHD-blob correlation in Fig. 8(b) have a more irregular timing and do not seem to correlate well with the MHD signal.

period of $\sim$260 μs (i.e., 3.8 kHz), while there is no clear oscillation in the cross-correlation function of the shot in (b). This demonstrates explicitly the correlation between the GPI peak radius Rpeak and B-dot signals in the shot in (a). The lag time of the peak in (a) is 60 μs, which depends on the exact phasing of the B-dot and GPI signals (see Sec. IV).

The conclusion from this section is that the GPI signal level and its peak radial position can be highly correlated with the low frequency coherent MHD. This is not too surprising since the GPI signal depends on the local electron density and temperature, which are modulated by the MHD (see Sec. IV B). What is surprising is that mesoscale blob formation can also be correlated with the large-scale MHD activity, as illustrated in Secs. III D and III E.

D. Large blob trajectories

In this section, we describe statistics and trajectories for large blobs for the two types of shots in Table I. The focus here is on comparing the set of seven shots with "high MHD-blob correlation" to the set of seven shots with "low MHD-blob correlation." As mentioned previously, the actual calculation of the MHD-blob correlations will be

discussed in Sec. III E, but for the moment, these datasets will be referred to this way without yet specifying the magnitude of these correlations.

Since there is no precise physics-based definition of a blob, the algorithm used to define and track blobs has varied with different diagnostics and applications. The simplified algorithm used for the present paper is described in detail in Appendix A. This algorithm focuses on *large amplitude* blobs with a normalized GPI signal amplitude threshold of at least 4 times the time-averaged value at the pixels of interest (i.e., T = 4), which attain a relatively large area of at least 14 cm^2 (N = 100 pixels) above the threshold sometime during its lifetime. This algorithm finds only the largest blob within the GPI frame at each time and follows this blob from its trigger time when at an area of 14 cm^2 back in time to its start at a small area (1.4 cm^2) and forward to its end at this same small area, as illustrated in frames #4–12 in Fig. 2(b). The normalized blob amplitude contours at T = 4 are fit by ellipses, and the ellipse centers are tracked vs time, as discussed in Appendix A.

Figure 6 shows the tracks of the centers of all large blobs within a 10 ms period for the shot with high MHD-blob correlation in (a)
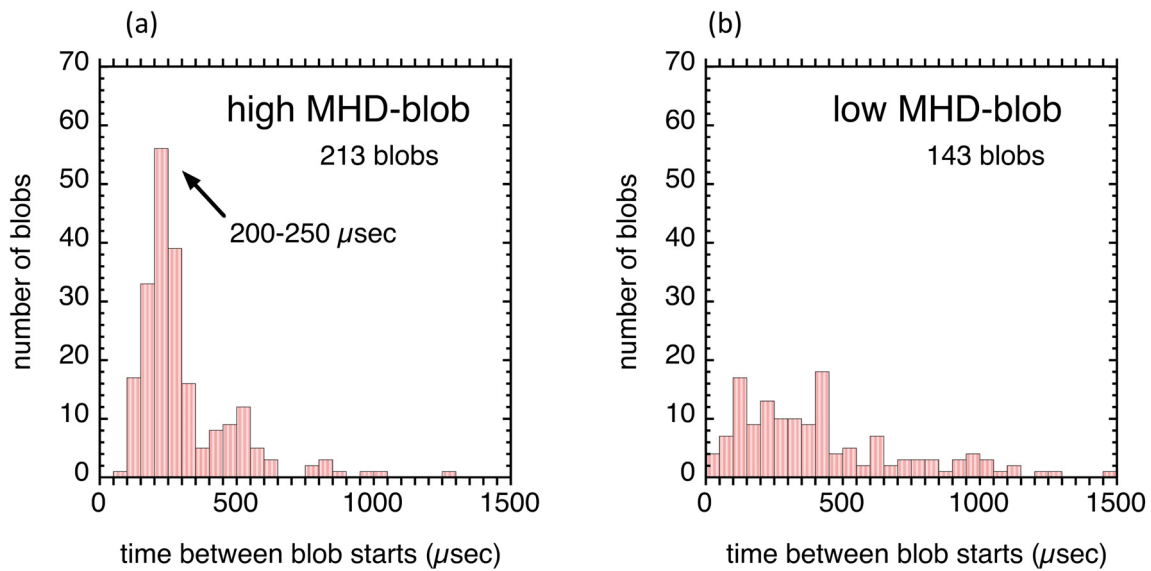
FIG. 9. Waiting time distribution between large blob triggers for the set of 7 similar shots with high and low MHD-blob correlations, using the same blob dataset as in Fig. 7. There is a clear peak in the waiting time distribution of Fig. 8(a) in the bins centered at 200–250 μs, which is consistent with the average frequency of the dominant MHD peak of 4.3 kHz in these seven shots (average period, 230 μs). For the case with low MHD-blob correlation in Fig. 8(b), there is no clear peak and only a broad waiting time distribution.

(#140390) and the shot with low MHD-blob correlation in (b) (#141749). This plot shows a map of the same GPI frames as in Fig. 2 but with the horizontal coordinate re-scaled as the radial distance with respect to the local separatrix (measured at the vertical center of the image) and the vertical scale as the relative poloidal (i.e., binormal) distance in this image. The start frame of each blob track is marked with a square symbol, and subsequent symbols in each blob track are separated by 1 frame time (2.5 μs). In case (a) with high MHD-blob correlation, there were 27 blob tracks (counting only blobs lasting more than three frames), each shown in a different color, and in case (b) with low MHD-blob correlation, there were 25 such tracks. All these blob tracks moved radially outward (to the right), and almost all

moved downward (ion diamagnetic drift direction). The dashed lines show the radial range over which the search was made for the blob trigger (see Appendix A).

The 27 large blob tracks for the shot with high MHD-blob correlation in Fig. 6(a) show a surprising self-consistency in their direction of motion, velocity, and radial location, compared to the shot with low MHD-blob correlation in Fig. 6(b). The trajectories with low MHD-blob correlation in Fig. 6(b) are considerably more diverse; for example, several blobs in Fig. 6(b) switch from nearly poloidal to nearly radial motion, and several blobs reverse their poloidal direction. The blobs with low MHD-blob correlation are also born nearer to the separatrix than in the case with high MHD-blob correlation.
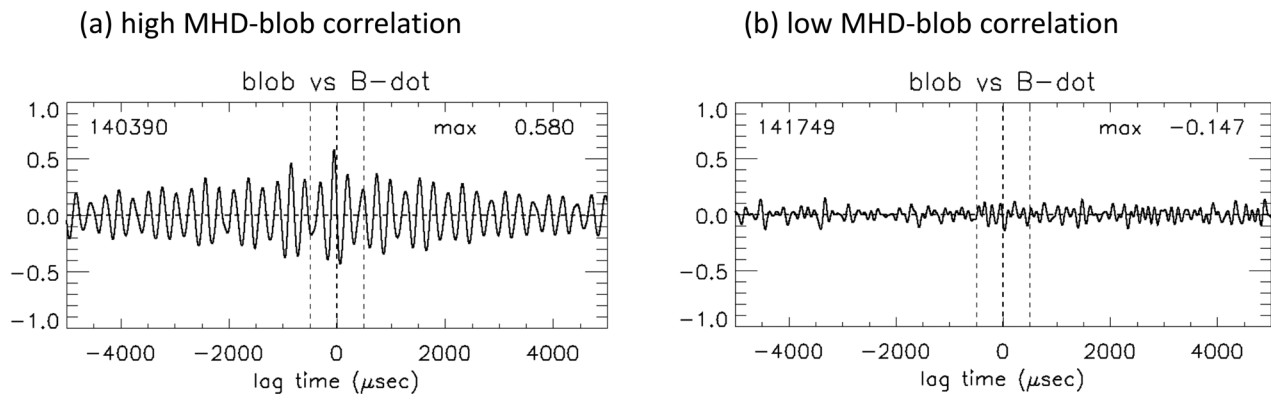
FIG. 10. The cross-correlation between the blob timing signals and the B-dot signals for the shots of Fig. 8. There is a clear modulation of the cross-correlation function at 3.8 kHz in (a) with high MHD-blob correlation, with a relatively high maximum cross-correlation coefficient of 0.58. However, there is no significant cross correlation in (b) with low MHD-blob correlation, with a maximum cross correlation of 0.15 (absolute value). These results look similar to those of Fig. 5 in which the GPI signal level was cross-correlated with the B-dot, but here the discrete blob signal is used for cross correlation with the B-dot.
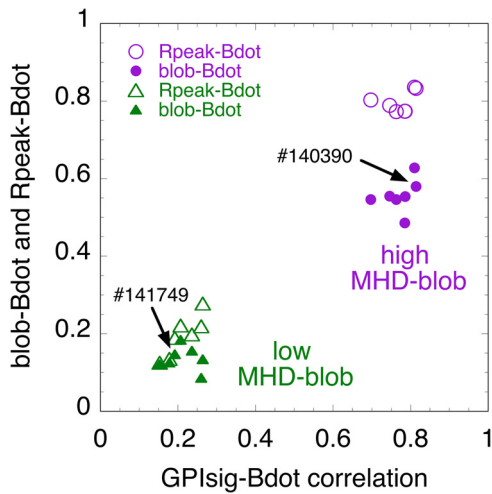
FIG. 11. The absolute values of the maximum of the cross-correlation functions for the three GPI vs B-dot cross-correlations, as evaluated within a lag time of $\pm 500\,\mu s$. The horizontal axis is the maximum cross correlation between the continuous GPI signal levels and the B-dot signal levels. The solid filled symbols show a maximum cross-correlation coefficient between the blob pulses and the B-dot signals, which for the seven shots with a high MHD-blob correlation was $0.56 \pm .04$ and for the seven shots with a low MHD-blob correlation was $0.14 \pm .03$. The open symbols show the maximum cross correlation between the Rpeak signals and the B-dot signals, which for the seven shots with a high MHD-blob correlation was 0.80 ± 0.03 and for the seven shots with a low MHD-blob correlation was 0.20 ± 0.05.

To check the results of Fig. 6(a) with a larger database, Fig. 7 shows the average radial and poloidal blob velocities for two sets of 7 similar shots, one set with high MHD-blob correlation including the shot in Fig. 6(a) (i.e., #140389–140395) and the other set with low

MHD-blob correlation including the shot in Fig. 6(b) (i.e., #141746, 47, 49, 51, and 54–56). All shots were analyzed exactly as in Fig. 6 with a blob amplitude trigger threshold of $T = 4$ and $N = 100$ pixels over a time period of 10 ms. Each point represents the average velocity evaluated from the start point to the end point of each blob, assuming that the radial is horizontal and the poloidal is vertical within the GPI image.

The seven shots with high MHD-blob correlation (purple) in Fig. 7 had a total of 210 blobs (with a lifetime > 3 frames), and the seven shots with low MHD-blob correlation (green) had a total of 152 blobs (> 3 frames). The average velocities are much more self-consistent for the shots with high MHD-blob correlation, as also seen in the trajectories of Fig. 6. The average blob velocities for the shots with high MHD-blob correlation were $V_{rad} = 0.69 \pm 0.13\,km/s$ and $V_{pol} = -0.86 \pm 0.31\,km/s$, and with low MHD-blob correlation, they were $V_{rad} = 0.80 \pm 0.43\,km/s$ and $V_{pol} = -1.8 \pm 1.2\,km/s$. The statistical variation (standard deviation) in these blob velocities was at least 3 times smaller for the shots with high MHD-blob correlation compared to the shots with low MHD-blob correlation, demonstrating the self-consistent motion of the large blobs for shots with high MHD-blob correlation. This self-consistency is even greater for larger blobs, as shown in Sec. IV E, since many of the blob velocities in Fig. 6(a) are somewhat higher shortly after their birth when these blobs are relatively small.

We note that some of the differences in blob trajectories of Fig. 7 between the two sets of seven shots were also seen in a previous paper,[38] in which the statistics of *all* (not just large) blobs were analyzed in the same two shots in the context of Ohmic vs H-mode plasmas. There the set of all blobs in the H-mode shots (with high MHD-blob correlation) also had a smaller spread in poloidal and radial velocities than the Ohmic shots (with low MHD-blob correlation) and perhaps more regular consistent
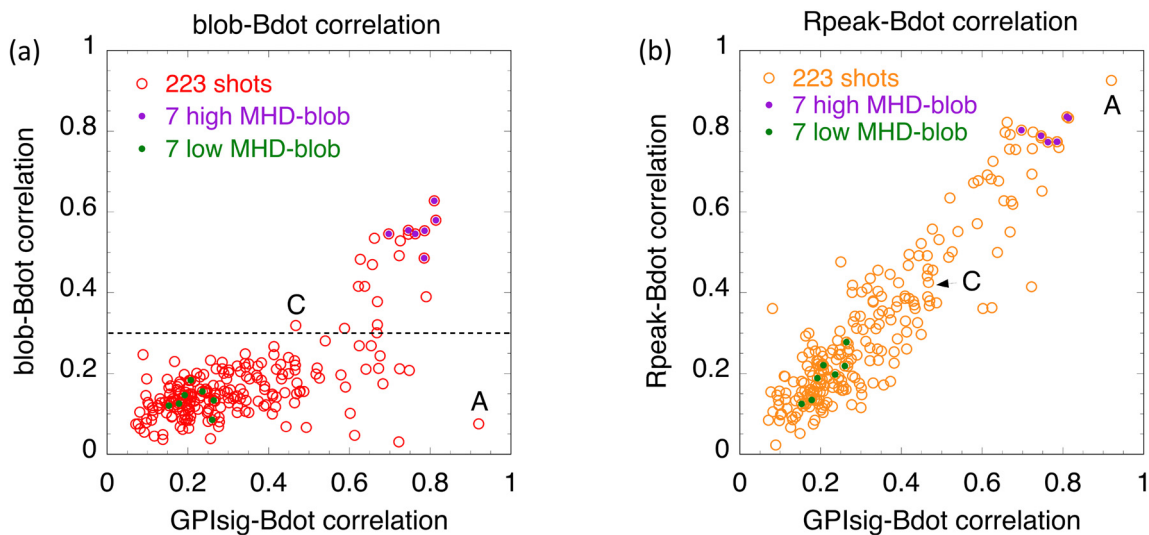
FIG. 12. Data from the wider database of 223 shots discussed in Sec. III G. In (a) is the blob-Bdot cross correlation vs the GPIsig-Bdot correlation, including the seven shots with high MHD-blob correlation marked in purple and the seven shots with low MHD-blob correlation marked in green. There are 21 shots with a significant cross-correlation level of 0.3, indicated by the dashed line. In (b) is the Rpeak-Bdot cross-correlation level for the same shots, showing a nearly linear relationship. The shots marked "A" and "C" are used as examples in Fig. 14.
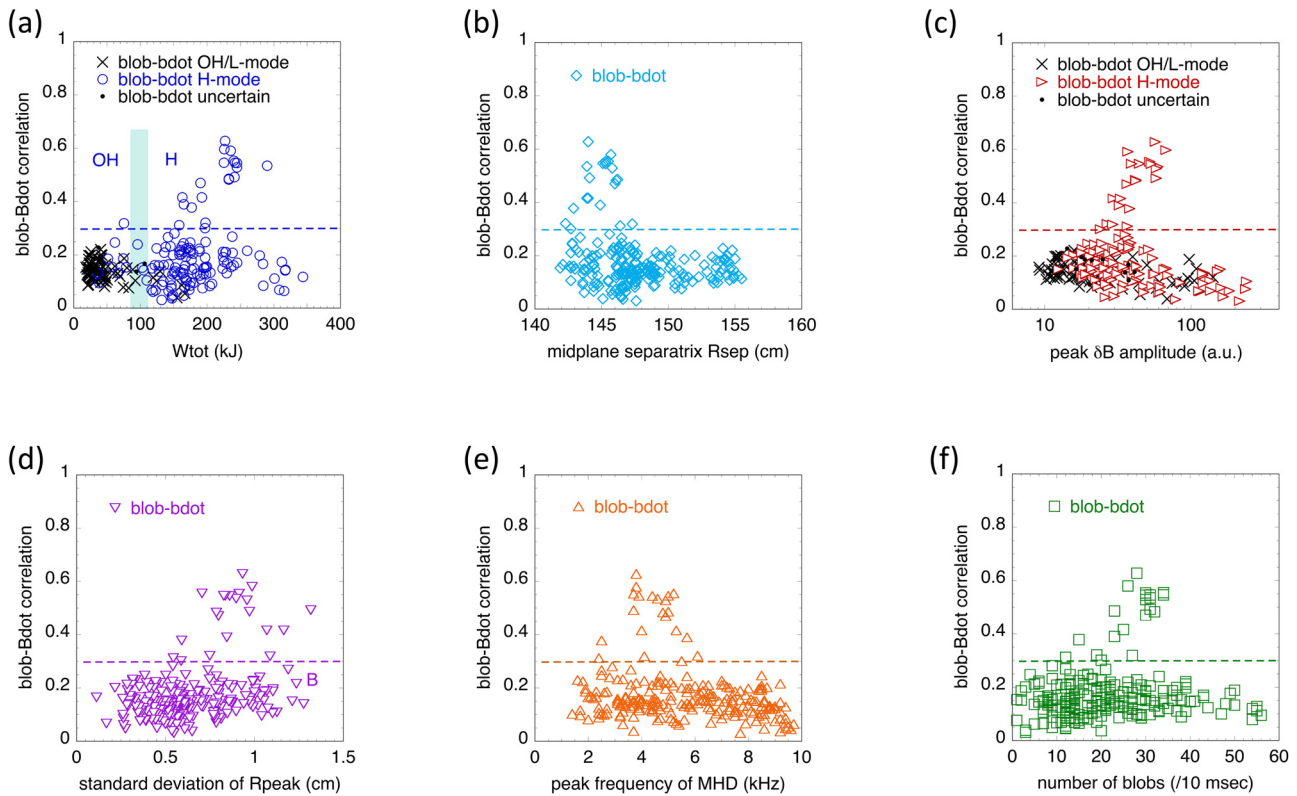
FIG. 13. Variations of the blob-Bdot cross-correlation coefficients on various parameters in the wider database of 223 shots. In (a) is the dependence on the total stored plasma energy Wtot (kJ) at the time of interest, in (b) is the dependence on the outer midplane separatrix radius R_{sep} (cm), and in (c) is the dependence on the amplitude of the peak magnetic fluctuation level. In (d) is the standard deviation of the fluctuations in the Rpeak radius over the 10 ms time of interest, in (e) is the peak MHD frequency in the range of 1–10 kHz, and in (f) is the number of large blobs detected in the 10 ms time of interest. In (a) and (b), the data are labeled as Ohmic or H-mode shots, with a few transitioning cases labeled as "uncertain."

trajectories. As mentioned in Sec. II, it was not noticed at the time of the previous paper that there was a correlation between MHD activity and blobs in these H-mode shots. As mentioned in Appendix A, the total number of *large* blob trajectories found in these seven shots was 210, whereas the total number of all blob trajectories analyzed in Ref. 38 was 820, so the present paper analyzed only the largest 25% of all blobs. Further analysis of the blob velocities as a function of the blob threshold amplitude is presented in Sec. III F, where it is shown that the spread in blob velocities becomes larger when the blob threshold level is reduced (Table II), consistent with the smaller spread in blob velocities in Fig. 7 compared with Ref. 38.
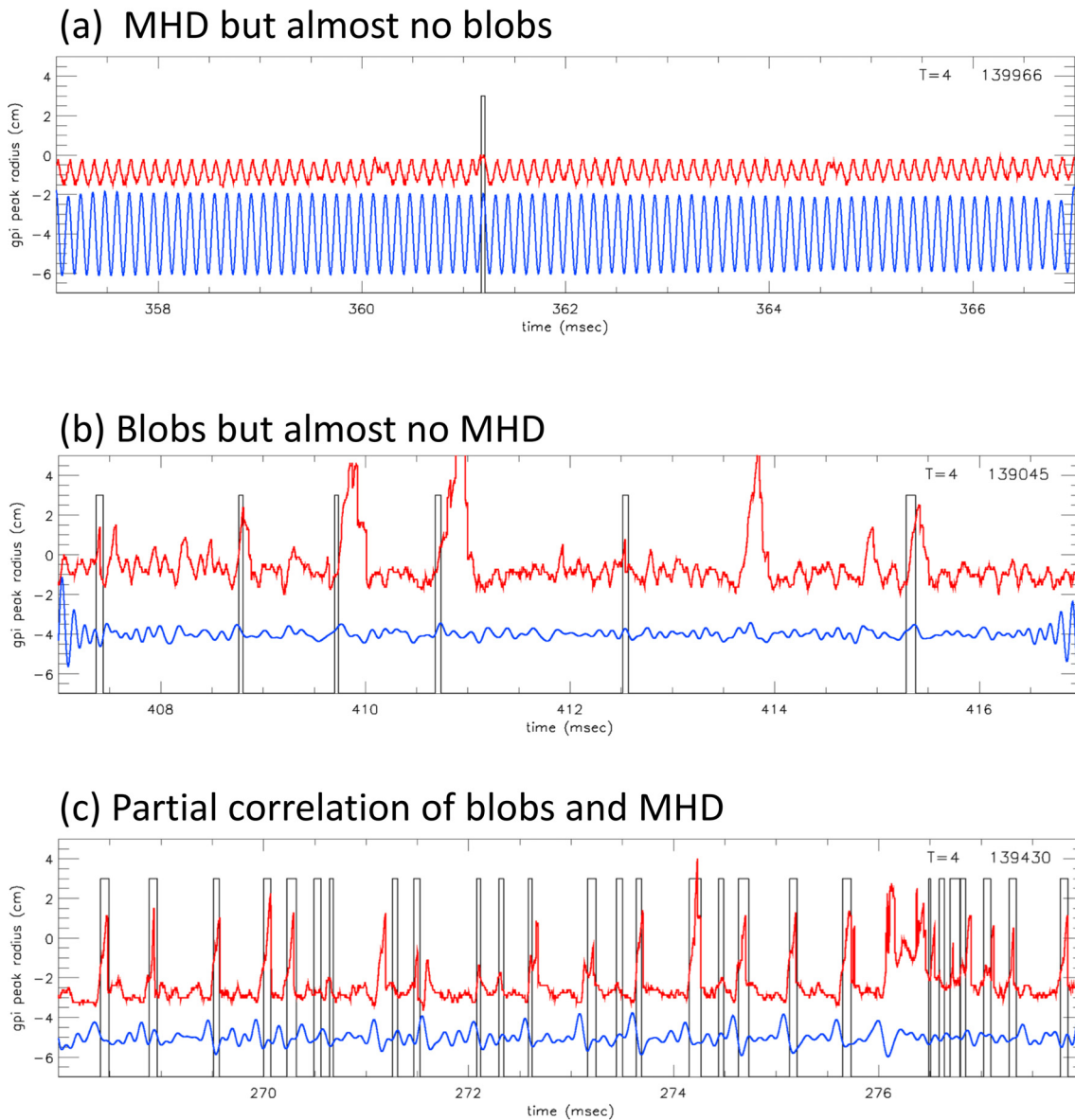
E. Correlation of large blobs with MHD

Figure 8 shows the start-to-end times for all the large blobs of Fig. 6 in the form of discrete on/off pulses (black), along with the GPI peak radial location "Rpeak" (red) and B-dot signals vs time (blue) for the shots with high MHD-blob correlation (#140390) and low MHD-blob correlation (#141749). This 1–10 kHz bandpass version of the B-dot signals shows the dominant 3.8 kHz mode in Fig. 4(a). Note that the blob start and end times are defined using a local amplitude

criterion for the normalized GPI signals (Appendix A), whereas the GPI peak radial location Rpeak is defined using the average values of the unnormalized GPI signals vs radius. Thus, the blob center motion can be entirely outward as in Fig. 6(a), while the Rpeak motion is oscillatory in radius as in Fig. 8(a).

The 27 large blobs in Fig. 8(a) with high MHD-blob correlation all occur during outward radial excursions in the Rpeak signal (red) and have a periodicity similar to the MHD signal (blue). However, some of the ~38 cycles of the B-dot signal did *not* contain large blobs, and occasionally, more than one blob occurred during an MHD cycle, such as, in the beginning, near 527.2 ms. The number of large blobs in the shot with high MHD-blob correlation was ~70% of the total number of dominant 3.8 kHz MHD mode periods. The 25 large blobs in the shot with low MHD-blob correlation in Fig. 8(b) are more irregular in time, although there still seems to be some correlation of the blob timing with the Rpeak signals.

Figure 9 shows the "waiting time" distribution between large blob trigger times for the set of seven shots with high MHD-blob correlations and seven shots with low MHD-blob correlation, using the same blob dataset as in Fig. 7. There is a clear peak in the waiting time distribution of Fig. 9(a) in the bin centered at 200–250 μs, which is consistent with the average frequency of the dominant MHD peak of

(a) MHD but almost no blobs

(b) Blobs but almost no MHD

## (c) Partial correlation of blobs and MHD

FIG. 14. Three examples of interesting shots in the wider database. Part (a) shows a shot with a large amplitude MHD signal but almost no blobs (shot labeled "A" in Fig. 12), part (b) shows a shot with large fluctuations in Rpeak and some blobs but almost no MHD signal activity [shot labeled "B" in Fig. 13(d)], and part (c) shows a shot with a marginal level of blob-Bdot correlation (shot labeled "C" in Fig. 12).

4.3 ± 0.7 kHz in these seven shots (average period, $230\,\mu s$). This suggests that the large blobs could be correlated with the MHD periodicity. For the case with low MHD-blob correlations in Fig. 9(b), there is no clear peak in the waiting time distribution.

The direct cross correlation between the start-to-end pulses of the large blobs and the B-dot signals for the two sample shots of Fig. 8 is shown explicitly in Fig. 10. There is a clear modulation in the cross-correlation function in the case of Fig. 10(a) at $\sim 260\,\mu s$ corresponding to the peak frequency of 3.8 kHz in this shot, with a maximum cross-correlation coefficient (within a lag time of $\pm 500\,\mu s$) of

0.58, which is relatively high. However, there is no clear correlation in the sample shot of Fig. 10(b), with a maximum cross correlation of -0.15. These results look similar to those of Fig. 5 in which the GPI signal level was cross-correlated with the B-dot signal, but in this case, the B-dot was correlated with the blob timing signal, which was a discrete on/off time series and not a continuous function.

It is important to note that the maximum possible cross-correlation between a discrete blob pulse signal and a continuous B-dot signal depends on the ratio of the blob lifetime to the MHD mode period and on the fraction of mode periods that do not have blobs, as
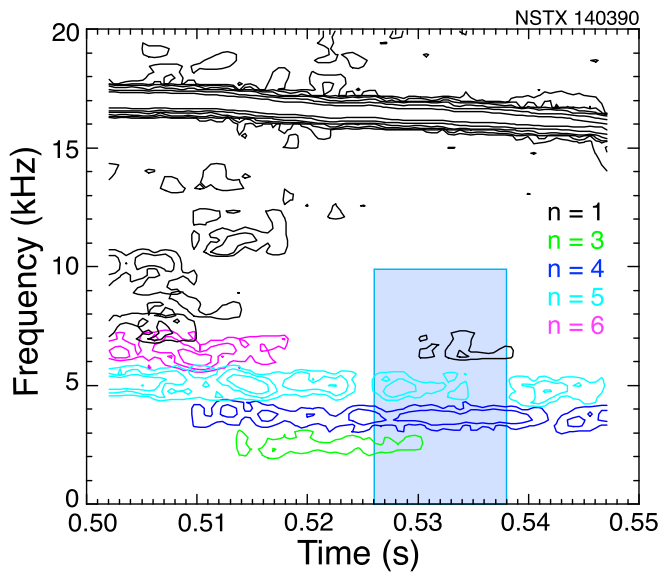
FIG. 15. Frequency spectrum of coherent modes in the B-dot coil signal used for analysis in this paper as a function of time. The time and frequency ranges of the GPI-MHD analysis are shown as a blue-shaded region. The dominant mode during this time is $n = 4$, with smaller features at $n = 1$, 3, and 5 in the frequency range of 1–10 kHz. There is also a strong $n = 1$ kink mode at 16 kHz, which is not included in the correlation analysis.

discussed in detail in Appendix B. For the case of the shot in Fig. 8(a), where the average blob duration was 82 μs for 27 blobs in this 10 ms period, the model of Appendix B would predict a blob-Bdot correlation of ~0.6, based on a blob lifetime/MHD period of 0.3 (82 μs/263 μs), and a fraction of periods without blobs of (12/38)= 30%.
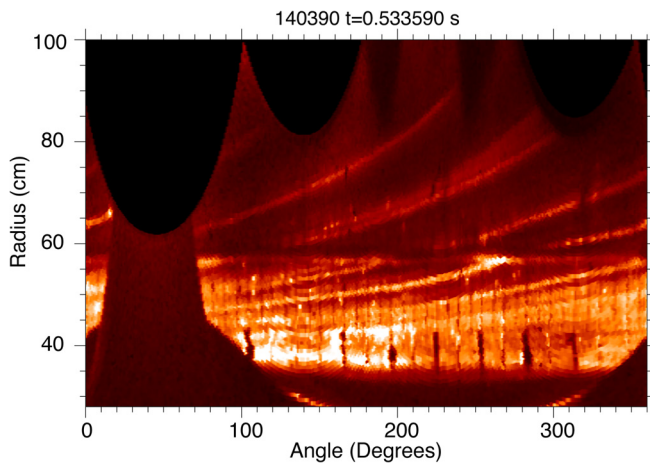
FIG. 16. Image of the lower divertor taken from a wide angle divertor camera using neutral lithium light with an 8 microsecond exposure and a 20 kHz framing rate. The divertor image was remapped as a function of the toroidal angle (horizontal axis) and divertor plate radius (vertical axis). The localization of neutral lithium emission to the divertor target plate surface enables the imaging of the intersection of the flux tubes perturbed by the MHD mode with the divertor target plate. In the divertor, the MHD mode appears as nested spirals (dominantly $n = 4$ at this time) rigidly rotating at the mode frequency. The outer strike point is at 36 cm.

Thus, the measured blob-Bdot correlation for this shot of 0.58 is close to that expected if the observed blobs were well correlated with a coherent B-dot signal.

Figure 11 shows a summary of the three main cross-correlations between the GPI data and the B-dot data based on the two shot groups of Figs. 7 and 9. Each point of Fig. 11 gives the absolute value of the maximum of the cross correlation as evaluated within a lag time of $\pm 500\,\mu$s. The horizontal axis is the maximum cross-correlation coefficient between the total GPI signal level "GPIsig" (after high pass filtering and normalization as in Fig. 2) and the B-dot signal, which indicates the overall extent of modulation of the GPI signal with the magnetic activity. For the seven shots with high MHD-blob correlation, the average cross correlation of the GPI signal with the B-dot was $0.77 \pm .04$, while for the seven shots with low MHD-blob correlation, this average was $0.21 \pm .04$. The solid filled symbols show a maximum cross-correlation coefficient between the discrete blob pulses and the B-dot signals, which for the seven shots with high MHD-blob correlation was $0.56 \pm .04$, while for the seven shots with low MHD-blob correlation, it was $0.14 \pm .03$. The open symbols show the maximum cross correlation between the Rpeak signals and the B-dot signals, which for the seven shots with high MHD-blob correlation was 0.80 ± 0.03, while for the seven shots with low MHD-blob correlation, this average was 0.20 ± 0.05. Thus, all three cross-correlations between the GPI signals and B-dot signals were significantly higher in the shots with high MHD-blob correlations.

It is interesting to determine how many large blobs are detected for each MHD period. For the seven shots with high MHD-blob correlation, the peak frequency of the MHD mode in the B-dot signals in the analysis range of 1–10 kHz varied from 3.7 to 5.2 kHz. The average number of blobs per MHD mode cycle varied from 0.46 to 0.81 in these shots, with an average of 0.69, and the average lifetime of the blobs varied from 68 to 83 μs, with an average of 73 μs. These average parameters can be put into the blob-MHD correlation model of Appendix B to predict the maximum possible blob-Bdot cross correlation. For an average blob lifetime per MHD period of 73 μs/230 μs ~0.3 and an average blob skip fraction of ~0.3, the expected blob vs B-dot cross correlation is ~0.6. This is close to the average blob-Bdot correlation of 0.56 ± 0.04, indicating that the blob-Bdot correlation was near to its maximum possible value for these shots.

The main conclusion from this subsection is that that there is a distinct difference in the large blob statistics and trajectories between shots with high and low MHD-blob correlations, as illustrated in Figs. 8(a) and 11. It is important to note that there is no reason why exactly one large blob should be seen at every cycle of MHD activity within this GPI field of view since this view covers only a range of poloidal angles ~11° wide just above the outer midplane. Also, the mechanism of the blob-MHD correlation is not yet clear, as discussed in Sec. IV.D.

F. Variations with blob threshold amplitude

The analysis of Secs. III D and III E focused specifically on large blobs with a normalized amplitude threshold of $T = 4$. For the sake of completeness, it is also interesting to see how the MHD-blob correlation varies with a larger or smaller blob amplitude threshold. Note that a choice of the amplitude threshold T in this analysis does not exactly define the blob amplitude, but only the minimum amplitude is used to trigger the blob tracking process. However, the average blob amplitude does increase with this threshold level. A study of the blob velocities vs blob amplitudes for Ohmic vs H-mode plasma was previously

TABLE II. Blob statistics vs blob threshold level T (seven shots with high MHD-blob correlation).

T (amplitude threshold)	# blobs[a] (average)	# short blobs[a]	V_{radial} (km/s)	$V_{poloidal}$ (km/s)	Blob vs. Bdot correlation
2	34	11	0.57 ± 0.22	-1.37 ± 1.2	0.33 ± 0.08
3	34	5	0.67 ± 0.12	-0.93 ± 0.40	0.54 ± 0.06
4	30	2	0.69 ± 0.13	-0.86 ± 0.31	0.56 ± 0.04
6	24	1	0.75 ± 0.14	-0.98 ± 0.27	0.52 ± 0.03
8	14	0	0.78 ± 0.13	-1.1 ± 0.26	0.40 ± 0.09

[a]per 10 ms period per shot.

reported in Ref. 38, although not specifically as a function of MHD activity.

The blob tracking analysis done for T = 4 in Sec. III D was redone for higher blob thresholds of T = 6 and T = 8 using the same seven shots with high MHD-blob correlation and the same pixel thresholds (e.g., triggering when there are N = 100 pixels above T). As shown in Table II, the total number of detected blobs (lasting ≥ 4 frames) decreased from 30 blobs/10 ms for T = 4 to a significantly lower 14 blobs/10 ms for T = 8. This is not surprising since the number of blobs generally decreases with their amplitude[38] and since the large blobs are also detected at the small amplitude thresholds. The average blob velocities at T = 8 (as defined in Sec. III D) became somewhat larger and even more self-consistent than at T = 4, with standard deviations of only $\pm 17\%$ in V_{rad} and $\pm 23\%$ in V_{pol}. However, the blob-MHD correlation coefficient was lower at T = 8 since there were only about half the number of blobs detected than at T = 4 (see Appendix B).

At the lowest blob threshold level of T = 2 in Table II, the blob tracks became more irregular, with larger variations in their velocity and smaller MHD-blob correlations than at T = 4. At this low threshold level, many of the triggered blobs were stopped short at <4 frames (as shown in the second column), mainly due to large jumps of the blob centers caused by the presence of other blobs in the same frame (see Appendix A). Thus, the highest correlation of the blobs with the Bdot signal occurred for blobs with T = 4, with somewhat lower correlations for T = 3 and T = 6. This motivated the assumption of T = 4 used for the analysis of Sec. III B–III E.

G. Wider database

Figure 12 shows the three GPI vs MHD cross-correlation coefficients as analyzed in Fig. 11 but now for a wider database of 223 shots (see Table I). These 223 shots were selected from the full 300 shot 2010 database of good GPI data, removing only shots with no magnetic sensor data (60 shots) and shots with no large blobs within the analysis time interval (21 shots).

The seven shots previously used for Figs. 7, 9, and 11 with high and low MHD-blob correlations are shaded in purple and green, respectively. As in Fig. 11, these plots show the absolute value of the maximum value of the blob-Bdot and Rpeak-Bdot cross correlations within a $\pm 500\,\mu s$ lag time, which corresponds to at least one period of the filtered B-dot signal range of 1–10 kHz. The blob events are all triggered as in Sec. III D at a threshold amplitude of T = 4 and area N = 100 pixels within the radial range outside the separatrix, but some shots have a larger separatrix radius and a smaller radial triggering

width. Shots with ELMs and other large transient events during the 10 ms times of interest have been excluded from this database.

The plot in Fig. 12(a) shows the maximum blob-Bdot cross correlation for the 223 shots vs the GPIsig-Bdot correlation coefficient (i.e., the relative influence of the MHD on the GPI signal level). The 7 points "with high MHD-blob correlation" previously used for Fig. 11 (purple dots) are among the shots with the largest blob-Bdot correlation in this database, and the 7 points "with low MHD-blob correlation" (shown with green dots) are in the group with a small blob-Bdot correlation. There are 21 shots (9%) with a significant level of blob-Bdot cross correlation above about 0.3 (dashed line) and 33 shots (15%) above a marginally significant correlation level of 0.23 (see Appendix B). About 17% of the 223 shots had high GPIsig-Bdot correlation levels of ≥ 0.5 (horizontal axis), and about 44% had a moderate GPIsig-Bdot correlation of ≥ 0.3. It is interesting that some shots have a high correlation between the GPI signal level "GPIsig" and the B-dot signal (i.e., ≥ 0.5 on the horizontal axis), but they do not have a high level of blob-Bdot correlation, such as point A discussed below.

The plot in Fig. 12(b) shows the cross-correlation coefficient between the fluctuations in the peak GPI radial location "Rpeak" and the B-dot fluctuations, again as a function of the correlation coefficient between the GPI signal level "GPIsig" and B-dot. The approximate linear dependence between these two correlations indicates that when the GPI signal level is strongly modulated by the MHD, there is also a high modulation in the peak GPI radial location. This is not too surprising since the MHD mode modulates the edge density and temperature, which modulates both the GPI signal and its radial location (see Sec. IV B).

Figure 13 shows variations in the blob-Bdot cross correlation with respect to several parameters in this wider database. The 21 shots with significant correlations are all located above the dashed lines at a correlation of 0.3. It is difficult to identify any clear parametric dependences in this database since most shots have blob-bdot correlation below the significant level.

Figure 13(a) shows that significant blob-Bdot correlation occurred only for shots in H-mode with relatively high stored energy W_{tot}, as discussed in more detail in the paragraph below. Figure 13(b) shows that the largest blob-Bdot correlations occur when the outer midplane separatrix radius is relatively far from the outer wall (i.e., at $R_{sep} = 141$–147 cm) and not close to the wall as for RF heated shots ($R_{sep} > 150$ cm). Figure 13(c) shows the blob-bdot correlation as a function of the amplitude of the peak magnetic fluctuation level of the MHD mode, as discussed in more detail in Sec. IV A. Figure 13(d) shows that the largest blob-Bdot correlations occur when the standard

deviation of the Rpeak radius fluctuations is ~1 ± 0.4 cm, i.e., with a peak-to-peak radial modulation of about 3 cm, as in Fig. 3(a). Figure 13(e) shows that the largest blob-Bdot correlations occur when the peak MHD frequency is ~3–6 kHz, i.e., well within the 1–10 kHz range over which the Bdot signal is analyzed. Finally, Fig. 13(f) shows that the largest blob-Bdot correlations occur when there are about 30 ± 5 blobs detected during the 10 ms analysis period, i.e., about 0.6 large blobs per MHD period (as discussed in Sec. III E).

Figure 13(a) shows that all 21 shots with a significant blob-bdot correlation level were in H-mode; however, most of the 137 shots in H-mode did not have a significant level of blob-bdot correlations. The reason why all high correlation shots were in H-mode is not yet clear. Higher edge gradients as seen in H-mode can drive MHD instability, but shots with the highest MHD level did not necessarily have the highest blob-bdot correlation, as shown in Fig. 13(c). The cause of the high blob-bdot correlation may have to do with the specific MHD mode spectrum, as discussed in Sec. IV A.

Other results from this database (not shown) are as follows: (a) the highest blob-Bdot cross-correlations occurred for an I/B ratio of ~0.15–0.2 MA/kG, which is in range when the GPI viewing angle is well-aligned along the local field line; (b) the highest blob-Bdot cross-correlations occurred at a moderate (i.e., not the highest) GPI signal level; and (c) the average blob lifetime was ~70 ± 8 µs for the shots with a blob-Bdot correlation of ≥0.3, which was somewhat higher than the 57 ± 15 µs average for the blob lifetime in all shots in the database, indicating that the blobs last somewhat longer for the shots with large MHD-correlated blobs. The average number of blobs per MHD period (i.e., inverse of peak frequency) for the 21 shots with the highest blob-Bdot cross correlation was ~0.6.

Figure 14 illustrates three examples of interesting shots in this wider database. Figure 14(a) shows shot "A" of Fig. 12(a), with 3 MW of NBI at B = 4.5 kG and I = 0.8 MA with 146 kJ of stored energy (#139966). This shot had the largest cross-correlation coefficient between the GPI signal modulation and the Bdot signal (0.92), and the largest cross correlation between the "GPIsig" and "Rpeak" signals (0.93) but had a very low blob-Bdot cross correlation (0.08). This shot had only one large blob and had a kink or tearing mode at ~8 kHz but no EHOs. Figure 14(b) shows the shot marked by "B" in Fig. 13(d), with 6 MW of NBI at B = 4.9 kG and I = 1.0 MA with 260 kJ of stored energy (#139045). This shot had one of the largest fluctuation levels in Rpeak (1.3 cm) but only a low level of blob-Bdot correlation (0.22), since even though there were six large blobs and several large radial excursions, there was no coherent MHD activity within 1–10 kHz in this case. Finally, Fig. 14(c) shows the shot marked by "C" in Fig. 12(a), with 0 MW of NBI (i.e., Ohmic) at B = 4.4 kG and I = 0.9 MA with 75 kJ of stored energy (#139430). This shot had a marginally significant level of blob-Bdot correlation (0.32) and GPIsig-Bdot correlation (0.47), with a complex spectrum of B-dot fluctuations within 1–10 kHz. This case seems to have some quasi-periodic blobs up to 276 ms (when there is small ELM) and illustrates a period of partial blob-Bdot correlation.

We note in closing that the present results on correlations between low frequency MHD and GPI are *not* related to the oscillations previously described as "quiet periods" in NSTX[41] or to the small amplitude oscillations observed in L-mode or before L-H transition in EAST, which were observed by Mirnov coils.[42] Those oscillations were associated with few kHz poloidal (i.e., zonal) edge flows just prior to

the L-H transition, whereas the present data showing blob-MHD correlations were observed in H-mode plasmas well after the L-H transitions. Note also that the MHD vs GPI correlations discussed in the present paper are also not related to ELMs since they occur during quasi-continuous MHD oscillations and not in periodic bursts.

IV. DISCUSSION

This section discusses in more detail some physical interpretations of these results. First, some properties of the MHD modes are described in Sec. IV A, and then, the relationship between the MHD and the GPI signals (not the blobs) is discussed in Sec. IV B. Section IV C contains a discussion of the 3D structure and motion of blobs vs MHD, Sec. IV D describes theoretical mechanisms for MHD-blob correlation, and Sec. IV E discusses experimental factors affecting the blob-MHD correlation.

A. Properties of the MHD activity

Figure 15 shows the coherent fluctuations vs time in the B-dot coil used to monitor the MHD activity for the sample shot with high MHD-blob correlation shown in Figs. 3–6 and 8 (#140390). The dominant toroidal mode number at the time of interest in the 1–10 kHz range (shaded blue region) is n = 4 at 3.8 kHz, with smaller n = 3 and 5 modes with a near constant frequency difference between the modes. This type of MHD activity appears to be similar to the edge harmonic oscillations (EHO) discussed previously for NSTX[32,33] and other devices,[34–36] which were toroidally rotating magnetic perturbations with multiple frequencies in the 1–10 kHz range. There is also a larger amplitude n = 1 kink mode at ~16 kHz, which was not correlated with GPI signal modulation or blob formation in this shot.

Another view of the toroidal mode structure for shot #140390 is shown in Fig. 16, which is an image of the lower divertor viewed in neutral lithium light taken from a wide angle divertor camera with an 8 µs exposure and a 20 kHz framing rate. The localization of neutral lithium emission to the divertor target plate surface enables the imaging of the intersection of the flux tubes perturbed by the MHD mode with the divertor target plate. The divertor image was remapped as a function of the toroidal angle and divertor radius, as described in Ref. 43. Similar patterns have been found previously for the divertor footprint of EHOs.[32,44] Those images show nested spirals with a periodic spatial structure like that of the MHD (n = 4, 5) moving with a constant toroidal velocity, *unlike* the intermittent and short lived (~100 µs) spirals due to midplane blobs that were previously seen to move radially outward in the SOL.[45] The dominant n = 4 toroidal mode can be seen in the upper part of this figure, where the flux surface corresponding to the GPI center is about 84 cm and the outer strike point separatrix is about 36 cm. The toroidal velocity of the n = 4 mode in this camera view is ~9 km/sec in the co-plasma current direction (NBI direction), which is the same as the toroidal n = 4 mode velocity determined by the Mirnov coils. Note that both this camera and B-dot coils measure only outside the separatrix, and so, they cannot directly determine the radial location of the mode inside the separatrix. Data from the NSTX reflectometers previously showed that EHO modes were localized within the steep pedestal gradient region just inside the separatrix of this type of H-mode plasma.[33]

The relationship between the peak MHD fluctuation amplitude δB and the blob-Bdot correlation is shown in Fig. 13(c) for the database of 223 shots. The 21 shots with a significant blob-Bdot correlation

>0.3 all had a moderately high δB amplitude, but there were also 30 shots with a *higher* peak magnetic fluctuation amplitude but a *smaller* blob-bdot correlation. Most of those 30 shots had a single large peak in the range of 1–10 kHz, such as shot #139966 in Fig. 14(a), which had a MHD kink or tearing mode but few blobs. Although H-mode shots tended to have a larger peak MHD level than Ohmic shots, there was no clear relationship between the peak magnetic fluctuation amplitude and the blob-bdot correlation.

A qualitative evaluation of the MHD mode spectrum was made for the 21 shots with the highest level of blob-MHD cross correlation in the wider database. Most shots (16/21) had EHO-like modes in the 1–10 kHz range, although the 2 shots with the strongest EHO modes did not have the highest blob-MHD correlations, and were not among the seven shots with high MHD-blob correlation of Fig. 12. Furthermore, in a few cases, kink modes were dominant in the 1–10 kHz range, and there were at least 8 shots in the wider GPI database, which had EHO-like modes, but no significant level of blob-Bdot correlations ($\sim$0.1–0.25). Thus, the connection between EHO-like modes and high blob-MHD correlation is not yet clear and requires further investigation.

B. Relationship of MHD and GPI (not blobs)

The most surprising new result of this paper was the high MHD-blob correlation in some shots, but it was also interesting that a significant fraction of the wider database of Sec. III G showed a high cross correlation between GPI signal modulation and MHD activity. About 17% of these shots had a high ($\geq$50%) correlation between the B-dot signal and both the GPI signal and its peak radius, and almost half the shots had a moderate GPIsig-Bdot correlation level ($\geq$30%), as shown in Fig. 12(b). These high GPIsig-Bdot correlations can occur without a significant blob-Bdot correlation, as shown, for example, by shot "A" in Fig. 11(a) and illustrated in Fig. 14(a).

Correlations between the edge MHD activity and GPI signals are not too surprising since the electron temperature and density are modulated by the MHD mode. Since the peak of the GPI (i.e., Dα) signals in NSTX plasmas occurs at Te = 100 eV,[46] the peak will move radially in phase with the local Te in the GPI gas cloud. The GPI emissivity at this peak depends on the local plasma density as modulated by the MHD and on the neutral density, which increases with the radius in the NSTX edge. Therefore, both the GPI Rpeak and its signal level GPIsig will be modulated by the edge MHD. For the 37 shots with a high ($\geq$50%) cross correlation between Rpeak and B-dot fluctuations, the average cross correlation between the Rpeak and GPIsig was very high (0.76), with an average lag time between the two of only 8 μs at peak correlation. Thus, for the shots with a high GPI-MHD correlation, the Rpeak radius was closely in phase with the GPI signal level, as expected from the above arguments. This relationship is also illustrated in Fig. 3(a).

Since, for cases with high MHD-blob correlations, there is also a high correlation between the B-dot signals and the Rpeak signals, it is interesting to consider whether this radial motion could cause the blob formation and therefore be the cause of the MHD-blob correlation. This is in fact the basis of two of the theoretical MHD-blob correlation mechanisms outlined in Sec. IV D. However, there are also clear cases in which outward Rpeak excursions are correlated with blob formation but in the shots with low MHD-blob correlation, as illustrated in Figs. 8(b) and 14(b). In these cases, the formation and outward motion of

the blob itself are apparently enough to cause the peak location of the GPI signal to move outward, independent of any MHD-induced radial motion. Thus, the Rpeak signal modulation cannot be viewed as a reliable indicator of the MHD-blob interaction.

C. 3D structure and motion of blobs vs MHD

It is well known that the structure of blobs is filamentary in 3D, i.e., with a very long correlation length in the direction parallel to the magnetic field in the tokamak scrape-off layer (SOL).[4] However, the full 3D blob structure cannot be resolved using GPI since it only measures the local radial vs poloidal structure at one toroidal location. It would be helpful to clarify the relationship between the 3D structure and motion of the large blobs discussed in this paper with their correlated MHD modes, especially since the blobs are on open field lines in the SOL, while the MHD modes are centered on closed field lines inside the separatrix.

One piece of information about this relationship is that the highest cross correlation between large blobs as seen in the GPI (just above the outer midplane) and the toroidal array of 10 B-dot coils (just below the outer midplane) was found for the B-dot coil nearest to the B-field line going through the GPI view, as illustrated in Fig. 1 and described in Sec. II. This was at first somewhat surprising since the MHD mode normally has a global mode structure. However, when there are multiple n-modes (as here), the phase of the total magnetic perturbation changes with the toroidal location, so the blobs can be best correlated with the MHD when both are near the same B-field line.

The perturbations in the SOL as seen in the camera (Fig. 16) rotate toroidally at the same velocity as the MHD mode in the plasma edge, as seen by the toroidal array of magnetic coils. The toroidal velocity of the dominant n = 4 mode in the SOL for a typical shot with MHD (#140390) is Vtor $\sim 2\pi*150$ cm$*3.8$ kHz/n $\sim$ 9 km/s in the co-current (and co-NBI) direction, as measured by both the outboard B-dot coils and the top-down camera. Thus, we *might* expect that the poloidal (i.e., binormal) velocity of the MHD mode perturbation as seen within the GPI viewing region (tilted at 36$°$ with respect to the toroidal direction) is Vpol $\sim$ 5 km/s. However, this is significantly larger than the measured poloidal velocity of the large blobs of Vpol = 0.82 $\pm$ 0.4 km/s downward (Fig. 7). Thus, the large blobs as seen in the SOL are at least somewhat decoupled from the ExB velocity of the MHD mode and not frozen with it, although both move downward in the ion diamagnetic direction.

This partial decoupling of the large blobs in the SOL from the MHD mode is also evident from the finite lifetime of the blobs ($\sim$75 μs), which is only a small fraction ($\sim$0.3) of the period of the dominant MHD mode, and from the unidirectional outward radial velocity of the blobs. Thus, the observed blobs may be viewed as filaments, which are "shaken off" by the MHD mode near the outer midplane separatrix and which then propagate into and through the SOL and are not frozen to the MHD mode. Although these large blobs are highly correlated with an outward movement of the GPI Rpeak signal, it is not yet clear at what phase of the MHD mode, the blob birth begins, or whether every cycle of the MHD mode creates a blob. The number of blobs observed in the GPI viewing region per mode cycle averaged $\sim$0.6 for the 21 shots with the best blob-MHD cross correlation, but less than half of the outer midplane is viewed by the GPI.

Finally, it is important to recall that the B-dot coils measure magnetic perturbations, whereas the GPI diagnostic measures mainly

density perturbations, so these fluctuations may not have the same origin. Possible physical relationships between these fluctuations are discussed in Sec. IV D.

D. Theoretical mechanisms for MHD-blob correlation

A single compelling explanation for the observed MHD-blob correlation is not yet apparent. Further data analysis and quantitative modeling of the phenomena are beyond the scope of this paper. However, in this section, we discuss a few possible mechanisms that could, in principle, correlate MHD modes and blob motion: (i) local pressure gradient increase, (ii) MHD mode acceleration, (iii) MHD mode radial velocity, (iv) MHD mode poloidal velocity and shear, and (v) unidirectional blob current.

(i) *Local pressure gradient increase*—The driving mechanism for blob propagation is generally attributed to curvature-induced charge polarization in the presence of the blob's internal pressure gradient.[1,4] This is essentially the well-known MHD interchange mechanism in a nonlinear blob-localized context. If a large-scale MHD mode is superimposed on the blob, then one might expect that the pressure gradient of the MHD mode would add to the internal pressure gradient of the blob, increasing the interchange drive and blob propagation velocity and/or perhaps triggering its emission in the first place. Indeed, avalanche-like processes for blob formation depending on local gradients have been proposed.[47,48]

(ii) *MHD mode acceleration*—If the MHD mode has a finite frequency in the plasma frame, then it will shake the field lines on which a nascent blob sits, back and forth in the radial direction. The emerging blob will experience this shaking as an acceleration of order $\delta a_{mhd} \sim \omega^2 \, \delta\xi_{rad}$, where ω is the MHD mode frequency and $\delta\xi_{rad}$ is the amplitude of the radial displacement caused by the MHD mode. If δa_{mhd} is comparable to the effective interchange acceleration for blob motion, $g = c_s^2/R$, then it is plausible that the MHD acceleration could induce emission of a blob when the phase of the MHD mode is such that δa_{mhd} adds to g. For present experiments, this mechanism seems too weak by at least an order of magnitude, even if the lab frame frequency is of order ω and $\delta\xi_{rad}$ was as large as a few cm. It could be relevant if one postulates a near-marginal condition for blob emission in the absence of the MHD mode.

(iii) *MHD mode radial velocity*—Distinct from the MHD-mode-induced pressure gradient, the MHD mode also provides an oscillating background flow on which the blob sits. Estimating the MHD radial velocity in the lab frame as $\delta V_{mhd,rad} = \omega \, \delta\xi_{rad}$, where $\omega \sim 2\pi \, 3.8 \times 10^3 \, s^{-1}$ is now the frequency in the lab frame, and estimating $\delta\xi_{rad} \sim 2$ cm [e.g., from Fig. 3(a), GPI peak radius], one finds a lab frame velocity of $\delta V_{mhd,rad} \sim 0.5$ km/s, which is significant compared with typical radial blob velocities shown in Fig. 7.

(iv) *MHD mode poloidal velocity and shear*—The MHD velocity perpendicular to **B** is given by $\delta E \times B$; therefore, $\delta V_{mhd,pol} \sim \delta V_{mhd,rad} (k_{rad}/k_{pol})$, where k_{rad} and k_{pol} refer to the MHD mode. Measurements of these wave-vectors are not available; however, since the mode has a low toroidal mode number and radial edge scale lengths are short, we expect $k_{rad}/k_{pol} > 1$, which would imply that $\delta V_{mhd,pol}$ could be up to a few km/s and significant compared with typical poloidal blob velocities shown in Fig. 7 (note that this poloidal velocity perturbation amplitude is distinct from the phase velocity of the mode discussed in Sec. IV C). Furthermore, if the radial scale length of $\delta V_{mhd,pol}$ is a few cm, then the shearing time $L_{rad}/\delta V_{mhd,pol}$ could be

of order 10 μs or less and thus potentially participate in the velocity shearing mechanism for blob formation.[9,11,49,50]

(v) *Unidirectional blob current*—Measurements on the MAST device[51] have shown that ELM filaments can carry a unidirectional parallel current of order 190 A, comparable to the filament cross-sectional area multiplied by the background plasma current density at the "birth" location of the filament. Subsequently, it was proposed that electromagnetic interactions of current-carrying filaments may influence their dynamics through $J \times B$ forces.[52] Direct measurements of field-aligned current filaments associated with blobs have also been made using magnetic probes in the RFX-Mod reverse field pinch[53] and in the simple magnetized torus TORPEX.[54] It is worth investigating whether similar currents in a blob-filament could interact with MHD mode currents and if such interaction could explain the observed correlations. The basic idea is that the parallel currents in the blob and the mode behave qualitatively as current-carrying parallel wires. Depending on the relative direction of the currents (i.e., phase of the MHD mode relative to the blob), an attractive or repulsive force exists on the blob, which, if large enough, could trigger its emission at the correct phase of the MHD mode. A rough order-of-magnitude estimate of the strength of this mechanism follows.

Based on the B-dot measurements and the B-dot coil separation from the plasma edge, it is estimated that the measured current perturbation during blob emission is on the order of 50 A. The force per unit length between current carrying wires with separation d is $F' = \mu_0 I_1 I_2/(2\pi d)$. Using the mass per unit length of a blob filament $m_i n_i \pi \delta_b^2$, where δ_b is the blob radius, we find the acceleration on the blob $a_I = \mu_0 I_1 I_2/(2\pi^2 d m_i n_i \delta_b^2)$, where I_1 and I_2 are the currents in the blob and MHD-mode. We do not have independent measurements of these individual currents. If we estimate $I_1 \sim I_2 = 50$ A, $n_e = 1. \times 10^{13}$ cm^{-3}, and $\delta_b = d = 3$ cm, then $a_I \sim 2.0 \times 10^{10}$ cm s^{-2}. This is competitive with $g = c_s^2/R \sim 6.4 \times 10^{10}$ cm s^{-2} obtained using $R = 150$ cm and $T_e = 20$ eV. We conclude that the electromagnetic force could plausibly be significant; if so, blob emission may be triggered by the mode, and conversely, the current in the blobs could locally enhance the mode. This might explain why blobs seem to be correlated with a particular phase of the B-dot signal, as seen in Fig. 8(a).

Of the mechanisms discussed here, (ii) seems to be the least likely explanation of the present observations, but the plausibility of the other proposed mechanisms will require testing with additional data, analysis, and modeling.

E. Experimental factors affecting MHD-blob decorrelation

There are several experimental factors, which could have caused some decorrelation of blobs and MHD in the analysis of Sec. III and which could be minimized in future experiments on this topic. First, the B-dot coil used for the cross-correlation analysis was not at the same location as the GPI viewing region, even though it had the best available alignment along the magnetic field (see Sec. II). For example, for shot #140390, the blob-MHD cross correlation decreased from 0.56 ± 0.04 for the best-aligned coil toroidally (shown in Fig. 2) to a slightly lower $0.50 \pm .04$ at 30° toroidally away at the same height (i.e., below the GPI gas puffer) and to about 0.4 about halfway around the machine. This shows that the MHD-blob correlation was moderately localized near the B-field line going through the GPI, probably due to

the multiple n-spectrum of modes. Ideally, the B-dot coil should be as close as possible to the GPI viewing region.

Second, the analysis time was arbitrarily chosen to be ±5 ms from the peak of the GPI signal, independent of the time evolution of the MHD modes in any particular shot. Ideally, the analysis time should be chosen to maximize the overlap with those MHD modes that are most likely to cause the blob-MHD correlation. Third, the limited GPI viewing region most likely missed many of the MHD-induced blobs since the average number of blobs observed per MHD mode period was only ~0.6 (see Sec. III E). Ideally, the blob diagnostic should cover the whole poloidal cross section, which would also help to identify the mechanism of MHD-induced blobs.

Finally, the available GPI database did not provide a systematic scan, which controlled the blob-MHD correlation. The available database scans shown discussed in Sec. III G and shown in Fig. 13 did not point to a plasma parameter that optimized this correlation. Ideally, new experiments can be designed specifically to test the theoretical mechanisms discussed in Sec. IV D.

V. SUMMARY AND CONCLUSIONS

This paper described a study of the cross correlations between edge fluctuations as seen in the GPI diagnostic and coherent low frequency magnetic fluctuations in NSTX (MHD). The main new result was that the presence of large blobs in the SOL was sometimes significantly correlated with MHD activity in the 3–6 kHz range. There were also many cases in which the GPI signal level and its peak radius Rpeak were highly correlated with the MHD activity but without any significant cross correlation with blobs.

The analysis of the GPI data for seven shots with high MHD-blob correlation showed that the large blobs moved downward in the SOL (ion diamagnetic direction) at $V_{pol} \sim 0.9$ km/s (Figs. 6 and 7), which is considerably less than $V_{pol} \sim 5$ km/s expected for the phase velocity of the MHD mode itself, based on its measured toroidal velocity. Thus, these large blobs in the SOL are at least somewhat decoupled from the MHD mode due to their differing poloidal velocity, as well as due to their outward radial velocity of $V_{rad} = 0.69$ km/s and their finite lifetime of 73 μs (see Sec. III E). For the 21 shots with significant MHD-blob correlations, there were ~0.6 blobs/MHD periods within the (limited) GPI field of view, which is roughly consistent with blobs being "shaken off" near the outer midplane during almost every MHD mode cycle.

As far as we know, there are no previous studies that showed a correlation as seen here between blobs and low frequency coherent magnetic fluctuations in a tokamak. It is interesting that many of the shots in the wider database with high MHD-blob correlation also appear to have multiple-mode structures similar to "EHO modes" (edge harmonic oscillations) previously reported in NSTX and other devices.[32–36] On the other hand, there were also shots with EHO-like modes but with only low MHD-blob correlations, so the connection between EHO-like modes and high blob-MHD correlation requires further investigation (see Sec. IV A).

Several theoretical mechanisms were discussed in Sec. IV D, which could potentially explain the observed MHD-blob correlation, namely, (i) local pressure gradient increase, (ii) MHD mode acceleration, (iii) MHD mode radial velocity, (iv) MHD mode poloidal velocity and shear, and (v) unidirectional blob current. Of these mechanisms, (ii) seems to be the least likely explanation of the present observations,

but the plausibility of the other proposed mechanisms will require testing with additional data, analysis, and modeling. Note that these mechanisms may apply to any edge MHD activity and are not specific to EHO modes.

Although edge particle and heat transport due to blobs was not discussed in this paper, it is plausible that this MHD-blob interaction may broaden the SOL heat flux width, as noted previously for EHO modes in NSTX,[32] or cause increased edge particle transport, as seen for EHO modes in DIII-D.[36] The enhanced creation of blobs with MHD during H-mode plasmas may also modify the ELM cycle in a way not presently incorporated into the theory of ELM stability. It may even be possible to intentionally create low frequency edge MHD modes to control the SOL transport and ELM cycle through this blob creation process.

There are a number of other open issues on the MHD-blob correlation, which should be followed up with further data analysis, experiment, and theory. The exact phasing of the blob birth with respect to the MHD mode structure could be determined by additional data analysis, which would help identify the MHD-blob coupling mechanism. The surprising self-consistency of the large blob tracks with MHD remains to be explained. An analysis of the expected MHD-induced modulation in the GPI signals could be done with a GPI simulation code like DEGAS 2,[46] assuming that the mode density and temperature perturbations are characterized. The magnetic perturbations due to the parallel currents in large blobs could be directly measured as done in Refs. 53 and 54, and their interaction and possible contribution to the MHD modes could be identified. Finally, the existing numerical simulations of blobs could be extended to include superimposed MHD modes, which could help clarify the physics of the interaction discussed in this paper.

APPENDIX A: BLOB TRACKING ALGORITHM

The blob tracking algorithm in the present paper is similar to that used in a previous paper on the NSTX blob structure and motion[38] but simplified to specifically detect the largest blobs. The first step is the same as before: the raw GPI image frames such as those in Fig. 1(a) are normalized to their time-average over the 10 ms analysis period. This removes the large-scale spatial variations within the field of view: for example, the radial variation due to the electron temperature profile and the poloidal variation due to the gas puff cloud shape and optical vignetting. These normalized
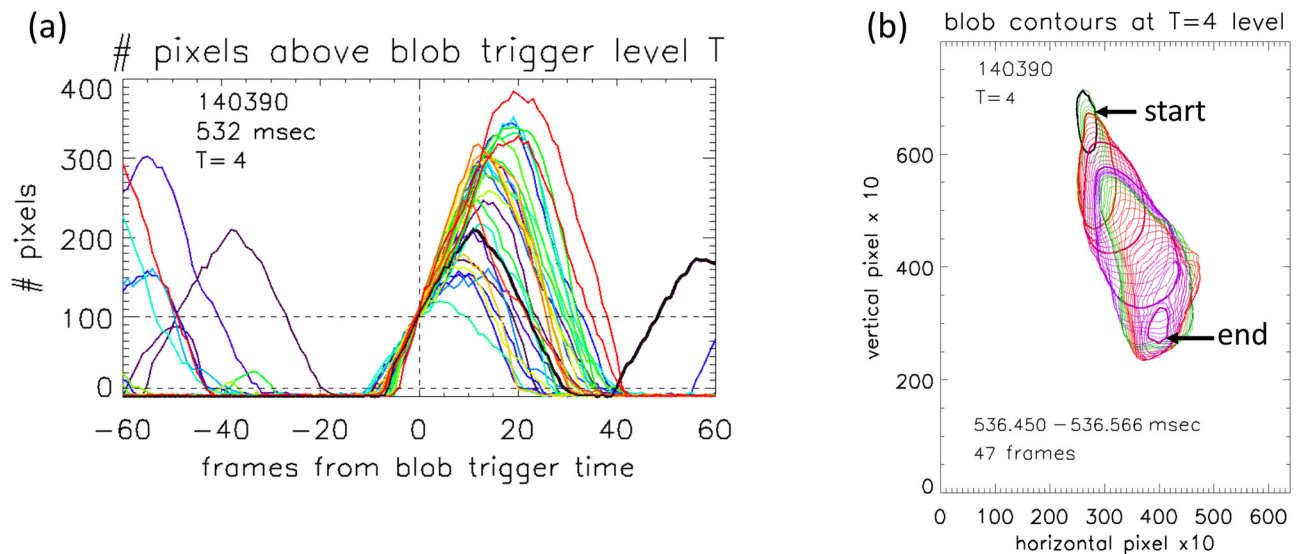
FIG. 17. Examples of the blob tracking algorithm as discussed in Appendix A. In (a), the vertical axis is the number of pixels per frame N above the chosen normalized trigger level (T = 4), and the horizontal axis is the relative time in frames from when this number crosses N = 100 (upper dashed line) to trigger a blob. For this shot, there were 27 blobs found within the analysis time of 532 ± 5 ms, as shown in the various colors. The blob start times and end times were determined when this number of pixels first falls below 10 (lower dashed line). Part (b) shows the calculated blob contours at the trigger level T = 4, with the start and stop and every fifth contour highlighted in darker lines. This blob changes the size and shape as it moves down and outward to the right, as also seen in the first blob in Fig. 2(b).

images were then smoothed over ±1 pixels (±0.4 cm) in both spatial directions and reduce pixilation at low signal levels. The resulting normalized images such as shown in Fig. 2(b) have a time-average value of 1.0 at each pixel and show more clearly the relative space-time variations due to the blobs.

The next steps focus on 2D tracking of the large blobs vs time. The blob trigger times are determined by inputting a desired normalized blob trigger level "T" and the number of pixels "N" above this level required for blob triggering. For example, choosing T = 4 and N = 100 pixels triggers on blobs which have a normalized signal level of 4× the time-averaged signal over in least 100 pixels in the 64 × 80 pixel frame, corresponding to an area of ∼14 cm^2 in the radial vs poloidal plane (N = 100 was used for all blobs in this paper). A blob threshold of T ≥ 4 is considered to be a large blob in this context. This blob trigger search is also constrained in the radial direction from the column nearest the separatrix to 30 columns outside this separatrix, i.e., over a radial range of ∼11 cm in the SOL (as shown in Fig. 6), or up to column 60 for shots with a larger separatrix radius.

To implement this blob triggering algorithm, the ∼4000 GPI frames (10 ms) for each shot are sequentially searched for all times when these conditions are marginally met, i.e., when the threshold of N = 100 pixels per frame above a normalized amplitude level T is crossed. Beginning at each of these blob trigger times, the start time for that large blob is then determined by going backward in time for up to 60 frames until the number of pixels above T falls below a specified lower limit of 10 pixels, corresponding to the smallest blob, which can be reliably identified (∼1.4 cm^2). Similarly, the end time for that blob is determined by going forward in time up to 60 frames from the blob trigger time until the

number of pixels with signal levels above T again falls below 10. Only blobs with ≥4 frames from start-to-end are retained for analysis.

An example of this process is shown in Fig. 17(a) for the blob trigger threshold T = 4 and N = 100 for shot #140390 (also used in Fig. 2). The vertical axis is the number of pixels in each frame above T = 4, and the horizontal axis is the relative time in frames from the blob trigger time (1 frame = 2.5 μs). For this shot, there were 27 blobs within the analysis time of 532 ± 5 ms, as shown in the various colors (corresponding to the colors in Fig. 6). All blobs were triggered when N = 100 was crossed (upper dashed line). The blob start times and end times were determined when the number of pixels above a T = 4 fell below 10 (lower dashed line). In this case, there was a clear separation in time between these large blobs and other blobs within ±60 frames (±150 μs).

The next step in this algorithm is to draw contour lines at the trigger level T within each frame from the blob start time to its end time, using the IDL "contour" function in a ×10 re-binned space of 640 × 800 pixels. This function identifies all contours at this level, but only the contour with the largest perimeter is used to identify the largest blob in each frame, which helps ensure that only a single large blob is followed as a function of time. An example of these contours for one blob is shown in Fig. 17(b), where the start and stop contours and every fifth frame are highlighted in darker lines. It is clear that that this blob contour changes the size and shape as it moves down and outward to the right, as was also evident from the normalized images this blob in Fig. 2(b). Each blob contour is then fit with an ellipse, which characterizes its center, axis size, area, ellipticity, and tilt angle, including contours, which are not completely closed within the field of view.

The final step in this algorithm is to start from the blob trigger and to halt the blob tracking if and when the center of the blob (i.e., center of the ellipse fit to its contour) jumps by more than 5 pixels per frame in the 2D GPI plane, corresponding to an inferred blob speed (7.5 km/s), above which the blob centroid is difficult to track reliably. This further ensures that the tracking does not jump from one blob to another and also eliminates the effect of occasional bad ellipse fits to the contours. The resulting smoothly varying tracks in Fig. 6 illustrate that a single blob was followed in each track.

As mentioned at the start of this section, the present blob tracking method is different than that used in the previous study of blobs in NSTX.[38] The main goal there was to study the overall statistics of the blob structure and its local velocity, including all blobs with a normalized amplitude of ≥ 1.5 (measured at half-height). In contrast, the present simplified algorithm follows only the largest blob in each frame with a normalized amplitude of (typically) $T \geq 4$, which at some trigger time attains an area of at least $N = 100$ pixels ($14\,\mathrm{cm}^2$). For comparison, the seven shots with high MHD-blob correlation used for Figs. 7 and 9 had a total of 210 large blob tracks at $T = 4$, whereas the same shots had a total of 820 blob tracks with the previous algorithm. Thus, the present study focuses on only the largest of the blobs studied previously.
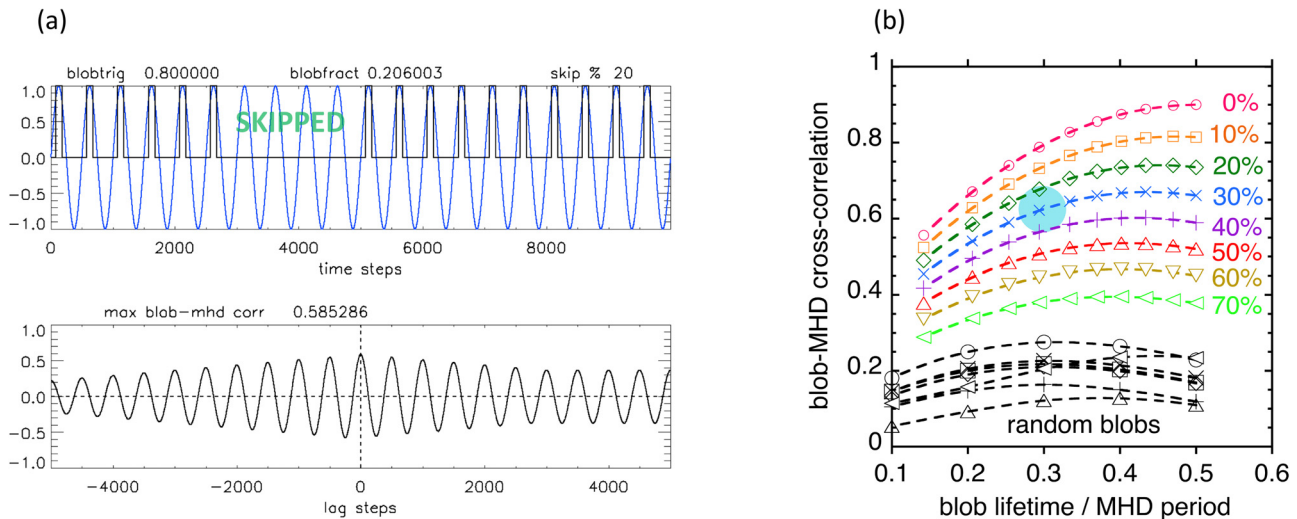
APPENDIX B: CROSS-CORRELATION OF CONTINUOUS MAGNETIC FLUCTUATIONS WITH DISCRETE BLOBS

The most interesting new result in this paper was a significant MHD-blob cross correlation between the magnetic B-dot fluctuation signal (a continuous function) and the blob timing signal (a discrete on/off or 1/0 function), as illustrated in Figs. 8 and 11.

Since cross-correlation functions are normally calculated between two continuous functions, this Appendix describes a numerical experiment which clarifies the use of this type of continuous vs discrete cross correlation.

A test case was chosen based on a sine wave proxy for an MHD signal with 20 periods in a 10 000 point time series. A blob timing signal ("1" state) was triggered only above a specified MHD signal amplitude, which was varied from $+0.0$ to $+0.9$ times the sine wave amplitude (i.e., only on positive-going MHD signals), as illustrated at the top of Fig. 18(a). The continuous MHD signal (blue) was then cross-correlated with the discrete blob (black) signal, as illustrated for one case at the bottom of Fig. 18(a), and the peak level of the time-delayed cross-correlation function was found as a function of the fractional time the blob signal was "on." The numerical results are shown in Fig. 18(b) as the top red "0%" curve. The resulting blob-MHD cross correlation decreased monotonically from 0.9 to 0.56 as the blob lifetime/MHD mode period (horizontal axis) decreased from 0.5 to 0.14, as expected, since for the zero blob width, the cross correlation should be zero.

Then, some fractions of the blob "on" signals were skipped (i.e., forced from 1.0 to 0.0), where this fraction was varied from 10% to 70%, as illustrated in Fig. 18(a) and summarized by the upper (colored) curves in Fig. 18(b) for various blob skip fractions (written at the right of each curve). With an increasing fraction of blob skips at a fixed blob lifetime/MHD period, the maximum cross correlation was lower, as expected, since for zero blobs, the correlation should be zero. For example, with 30% blob skips, as for the seven shots with high MHD-blob correlation in Fig. 11 (see Sec. III E) and for the observed blob lifetime/MHD period of ~0.3, the expected maximum cross-correlation coefficient was ~0.6 (blue circled region). The measured blob-Bdot cross correlation for these

FIG. 18. Numerical test case for the cross correlation between a continuous sine wave and a discrete blob pulse timing signal as discussed in Appendix B. A typical test case is shown in part (a), with blobs occurring only above an MHD signal level of 0.8, corresponding to a blob lifetime/MHD period =0.21 and with 4/20 = 20% of blobs "skipped," resulting in a peak cross correlation of 0.59. In part (b), the peak cross-correlation results are shown for various blob lifetime/MHD period fractions and skip fractions. The colored curves are labeled with the fractions of blobs skipped, with 0% for no skips (one blob per MHD period). The results for this blob model are shown in color, and random blobs are shown in black. The blue circle region corresponds to the data for the seven shots with large MHD-blob correlations discussed in Sec. III E.

seven shots with high MHD-blob correlation was 0.56 ± 0.04 (Fig. 11), approximately consistent with this blob model result. In this model, the maximum cross correlation occurs at zero time lag, but for the actual measured data, the maximum correlation was evaluated within a time lag of $\pm 500 \mu s$, to allow for a variable blob-Bdot phase of at least one MHD period.

The same model was applied using randomly timed blobs in order to find the level of the random cross correlation between blobs and a sinusoidal B-dot signal, with results shown in black curves at the bottom of Fig. 18(b). The symbols represent the same skip fractions as above. The result was that all random cross-correlations within the ranges of (blob lifetime/MHD period) = 0.1–0.5 and skip fractions of 0.0–0.7 were below 0.3, and the random cross correlation for a skip fraction of 0.3 and (blob lifetime/MHD period)=0.3 was 0.23. Thus, a cross correlation level of 0.3 is used in Sec. III G to identify statistically significant blob-Bdot cross-correlations in the wider database.

REFERENCES

[1]S. I. Krasheninnikov, Phys. Lett. A **283**, 368 (2001).
[2]J. A. Boedo, D. Rudakov, R. Moyer, S. Krasheninnikov, D. Whyte, G. McKee, G. Tynan, M. Schaffer, P. Stangeby, P. West, S. Allen, T. Evans, R. Fonck, E. Hollmann, A. Leonard, A. Mahdavi, G. Porter, M. Tillack, and G. Antar, Phys. Plasmas **8**, 4826 (2001).
[3]S. J. Zweben, J. A. Boedo, O. Grulke, C. Hidalgo, B. LaBombard, R. J. Maqueda, P. Scarin, and J. L. Terry, Plasma Phys. Controlled Fusion **49**, S1 (2007).
[4]D. A. D'Ippolito, J. R. Myra, and S. J. Zweben, Phys. Plasmas **18**, 060501 (2011).
[5]G. S. Xu, V. Naulin, W. Fundamenski, C. Hidalgo, J. A. Alonso, C. Silva, B. Goncalves, A. H. Nielsen, J. Juul Rasmussen, S. I. Krasheninnikov, B. N. Wan, M. Stamp, and JET EFDA Contributors. Nucl. Fusion **49**, 092002 (2009).
[6]L. W. Yan, J. Cheng, W. Y. Hong, K. J. Zhao, J. Qian, Q. W. Yang, J. Q. Dong, X. R. Duan, and Y. Liu, J. Nucl. Mater. **415**, S475 (2011).
[7]J. R. Myra, D. A. D'Ippolito, D. P. Stotler, S. J. Zweben, B. P. LeBlanc, J. E. Menard, R. J. Maqueda, and J. Boedo, Phys. Plasmas **13**, 092509 (2006).
[8]G. Fuchert, G. Birkenmeier, M. Ramisch, and U. Stroth, Plasma Phys. Control Fusion **58**, 054005 (2016).
[9]I. Furno, F. Avino, A. Bovet, A. Diallo, A. Fasoli, K. Gustafson, D. Iraji, B. Labit, J. Loizu, S. H. Muller, G. Plyushchev, M. Podesta, F. M. Poli, P. Ricci, and C. Theiler, J. Plasma Phys. **81**, 345810301 (2015).
[10]S. I. Krasheninnikov, Phys. Lett. A **380**, 3905 (2016).
[11]N. Bisai, S. Banerjee, and A. Sen, Phys. Plasmas **26**, 020701 (2019).
[12]P. W. Gingell, S. C. Chapman, and R. O. Dendy, Plasma Phys. Control Fusion **56**, 035012 (2014).
[13]J. R. Myra, D. A. Russell, D. A. D'Ippolito, J.-W. Ahn, R. Maingi, R. J. Maqueda, D. P. Lundberg, D. P. Stotler, S. J. Zweben, J. Boedo, M. Umansky, and NSTX Team, Phys. Plasmas **18**, 012305 (2011).
[14]P. Paruta, C. Beadle, P. Ricci, and C. Theiler, Phys. Plasmas **26**, 032302 (2019).
[15]A. Ross, A. Stegmeir, P. Manz, D. Groselj, W. Zholobenko, D. Coster, and F. Jenko, Phys. Plasmas **26**, 102308 (2019).
[16]J. R. Angus and M. V. Umansky, Phys. Plasmas **21**, 012514 (2014).
[17]L. Easy, F. Militello, J. Omotani, N. R. Walkden, and B. Dudson, Phys. Plasmas **23**, 012512 (2016).
[18]R. M. Churchill, C. S. Chang, S. Ku, and J. Dominski, Plasma Phys. Controlled Fusion **59**, 105014 (2017).
[19]H. Hasegawa and S. Ishiguro, Phys. Plasmas **22**, 102113 (2015).
[20]A. S. Thrysøe, L. E. H. Tophøj, V. Naulin, J. J. Rasmussen, J. Madsen, and A. H. Nielsen, Plasma Phys. Controlled Fusion **58**, 044010 (2016).
[21]D. A. Russell, J. R. Myra, and D. P. Stotler, Phys. Plasmas **26**, 022304 (2019).
[22]N. Bisai and P. K. Kaw, Phys. Plasmas **25**, 012503 (2018).
[23]S. I. Krasheninnikov and A. I. Smolyakov, Phys. Plasmas **14**, 102503 (2007).
[24]A. I. Smolyakov and S. I. Krasheninnikov, Phys. Plasmas **15**, 072302 (2008).
[25]G. Y. Antar, J. H. Yu, and G. Tynan, Phys. Plasmas **14**, 022301 (2007).
[26]B. J. Ding, G. L. Kuang, J. F. Shan, G. S. Xu, M. Song, B. N. Wan, Y. P. Zhao, and J. G. Li, Plasma Phys. Controlled Fusion **46**, 1467 (2004).
[27]Y. Xu, R. R. Weynants, M. Van Schoor, M. Vergote, S. Jachmich, M. W. Jakubowski, M. Mitri, O. Schmitz, B. Unterberg, P. Beyer, D. Reiser, K. H. Finken, M. Lehnen, and TEXTOR Team. Nucl. Fusion **49**, 035005 (2009).
[28]T. Wu, L. Nie, M. Xu, J. Yang, Z. Chen, Y. Shi, N. Wang, D. Li, R. Ke, Y. Yu, S. Gong, T. Long, J. Chen, B. Liu, and J-TEXT Team, Plasma Sci. Technol. **21**, 125102 (2019).
[29]N. Vianello, C. Rea, M. Agostini, R. Cavazzana, G. Ciaccio, G. De Masi, E. Martines, A. Mazzi, B. Momo, G. Spizzo, P. Scarin, M. Spolaore, P. Zanca, M. Zuin, L. Carraro, P. Innocente, L. Marrelli, M. E. Puiatti, D. Terranova, and RFX-mod Team, Plasma Phys. Controlled Fusion **57**, 014027 (2015).
[30]L. Bardoczi, T. L. Rhodes, A. Banon Navarro, C. Sung, T. A. Carter, R. J. La Haye, G. R. McKee, C. C. Petty, C. Chrystal, and F. Jenko, Phys. Plasmas **24**, 056106 (2017).
[31]A. Poye, O. Agullo, M. Muraglia, X. Garbet, S. Benkadda, A. Sen, and N. Dubuit, Phys. Plasmas **22**, 030704 (2015).
[32]K. F. Gan, J.-W. Ahn, T. K. Gray, S. J. Zweben, E. D. Fredrickson, F. Scotti, R. Maingi, J.-K. Park, G. P. Canal, V. A. Soukhanovskii, A. G. Mclean, and B. D. Wirth, Nucl. Fusion **57**, 126053 (2017).
[33]J.-K. Park, R. J. Goldston, N. A. Crocker, E. D. Fredrickson, M. G. Bell, R. Maingi, K. Tritz, M. A. Jaworski, S. Kubota, F. Kelly, S. P. Gerhardt, S. M. Kaye, J. E. Menard, and M. Ono, Nucl. Fusion **54**, 043013 (2014).
[34]E. R. Solano, P. J. Lomas, B. Alper, G. S. Xu, Y. Andrew, G. Arnoux, A. Boboc, L. Barrera, P. Belo, M. N. A. Beurskens, M. Brix, K. Crombe, E. de la Luna, S. Devaux, T. Eich, S. Gerasimov, C. Giroud, D. Harting, D. Howell, A. Huber, G. Kocsis, A. Korotkov, A. Lopez-Fraguas, M. F. F. Nave, E. Rachlew, F. Rimini, S. Saarelma, A. Sirinelli, S. D. Pinches, H. Thomsen, L. Zabeo, and D. Zarzoso, Phys. Rev. Lett. **104**, 185003 (2010).
[35]C. J. Lasnier, K. H. Burrell, J. S. deGrassie, A. W. Leonard, R. A. Moyer, G. D. Porter, J. G. Watkins, and DIII-D Team, J. Nucl. Mater. **313–316**, 904 (2003).
[36]K. H. Burrell, T. H. Osborne, P. B. Snyder, W. P. West, M. E. Fenstermacher, R. J. Groebner, P. Gohil, A. W. Leonard, and W. M. Solomon, Nucl. Fusion **49**, 085024 (2009).
[37]S. J. Zweben, W. M. Davis, S. M. Kaye, J. R. Myra, R. E. Bell, B. P. LeBlanc, R. J. Maqueda, T. Munsat, S. A. Sabbagh, Y. Sechrest, D. P. Stotler, and NSTX Team, Nucl. Fusion **55**, 093035 (2015).
[38]S. J. Zweben, J. R. Myra, W. M. Davis, D. A. D'Ippolito, T. K. Gray, S. M. Kaye, B. P. LeBlanc, R. J. Maqueda, D. A. Russell, D. P. Stotler, and NSTX Team, Plasma Phys. Controlled Fusion **58**, 044007 (2016).
[39]S. J. Zweben, D. P. Stotler, F. Scotti, and J. R. Myra, Phys. Plasmas **24**, 102509 (2017).
[40]S. J. Zweben, J. L. Terry, D. P. Stotler, and R. J. Maqueda, Rev. Sci. Instrum. **88**, 041101 (2017).
[41]S. J. Zweben, R. J. Maqueda, R. Hager, K. Hallatschek, S. M. Kaye, T. Munsat, F. M. Poli, A. L. Roquemore, Y. Sechrest, and D. P. Stotler, Phys. Plasmas **17**, 102502 (2010).
[42]L. M. Shao, G. S. Xu, 2, R. Chen, L. Chen, G. Birkenmeier, Y. M. Duan, W. Gao, P. Manz, T. H. Shi, H. Q. Wang, L. Wang, M. Xu, N. Yan, L. Zhang, and EAST Team, Plasma Phys. Controlled Fusion **60**, 035012 (2018).
[43]F. Scotti, A. L. Roquemore, and V. A. Soukhanovskii, Rev. Sci. Instrum. **83**, 10E532 (2012).
[44]F. Scotti, V. A. Soukhanovskii, J.-W. Ahn, A. G. McLean, and R. Kaita, Nucl. Mater. Energy **12**, 768 (2017).
[45]F. Scotti, S. Zweben, J. Myra, R. Maqueda, and V. Soukhanovskii, Nucl. Fusion **60**, 026004 (2020).
[46]D. P. Stotler, F. Scotti, R. E. Bell, A. Diallo, B. P. LeBlanc, M. Podestà, A. L. Roquemore, and P. W. Ross, Phys. Plasmas **22**, 082506 (2015).
[47]D. E. Newman, B. A. Carreras, P. H. Diamond, and T. S. Hahm, Phys. Plasmas **3**, 1858 (1996).
[48]Y. Sarazin and P. Ghendrih, Phys. Plasmas **5**, 4214 (1998).
[49]I. Furno, B. Labit, A. Fasoli, F. M. Poli, P. Ricci, C. Theiler, S. Brunner, A. Diallo, J. Graves, M. Podestà, and S. H. Müller, Phys. Plasmas **15**, 055903 (2008).
[50]N. Bisai, A. Das, S. Deshpande, R. Jha, P. Kaw, A. Sen, and R. Singh, Phys. Plasmas **12**, 102515 (2005).

[51]A. Kirk, N. Ben Ayed, G. Counsell, B. Dudson, T. Eich, A. Herrmann, B. Koch, R. Martin, A. Meakins, S. Saarelma, R. Scannell, S. Tallents, M. Walsh1, H. R. Wilson, and MAST Team, Plasma Phys. Controlled Fusion **48**, B433 (2006).

[52]J. R. Myra, Phys. Plasmas **14**, 102314 (2007).

[53]M. Spolaore, N. Vianello, M. Agostini, R. Cavazzana, E. Martines, P. Scarin, G. Serianni, E. Spada, M. Zuin, and V. Antoni, Phys. Rev. Lett. **102**, 165001 (2009).

[54]I. Furno, M. Spolaore, C. Theiler, N. Vianello, R. Cavazzana, and A. Fasoli, Phys. Rev. Lett. **106**, 245001 (2011).